Understanding the Chromatographic Processing of Recombinant Human Papillomavirus Vaccine Using Ceramic Hydroxyapatite

---

A Thesis

Presented to

the faculty of the School of Engineering and Applied Science

University of Virginia

---

in partial fulfillment

of the requirements for the degree

Master of Science

by

Yiran Wang

December

2016

APPROVAL SHEET

The thesis

is submitted in partial fulfillment of the requirements

for the degree of

Master of Science

AUTHOR

The thesis has been read and approved by the examining committee:

Giorgio Carta

Advisor

Steven Caliari

Michael L. King

Accepted for the School of Engineering and Applied Science:

Craig H. Benson, Dean, School of Engineering and Applied Science

December

2016

Abstract

Virus like particles (VLPs) are novel biopharmaceutical products that have become widely used for vaccines, gene therapy and immunotherapy. The purification of VLPs poses several unique challenges including the handling of their large molecular size and the removal of nucleic acid contaminants. Ceramic hydroxyapatite (CHT), a mixed-mode chromatography adsorbent, has shown promise in purifying VLPs from nucleic acid due to its multimodal adsorption mechanism. This work has two principal objectives. The first is to investigate the interaction of RNA with VLPs using biolayer interferometry (BLI) measurements. Biotin tagged-RNA is immobilized on a streptavidin-coated biosensor and the VLP is immobilized through carboxyl-amine electrostatic interaction. The BLI observations show that VLP variants have different RNA association responses, which are also dependent on the buffer composition. The second objective focuses on characterizing CHT and evaluating its performance as a possible candidate for purifying VLPs and RNA removal. Confocal laser scanning microscopy (CLSM) with fluorescent labeling was used to visualize the adsorption behavior of both components. This work helps elucidates the mechanism of RNA association with VLPs and facilitates the design of new strategies for the next generation of VLP purification processes.

Acknowledgements

I would like to thank my advisor Giorgio Carta for his advice and inspiration on my project. I also want to thank my advisory committee members, Dr. Steven Caliari and Dr. Michael L. King. I would like to thank Dr. Dicky Abraham from Merck & Co., for providing the financial support for my research and industrial insights relevant to this study. I would like to thank all my group members, Mimi Zhu, Jason Reck, Arch Creasy, Preston Fucks, Andreas Alberti, Joey Roberts and Lucas Kimerer and the alumni, Yige Wu, Shaojie Zhang and Jing Guo. I would have never been able to get through this project without your encouragement and instruction.

I also want to thank my parents and all my friends for their kind support. Thank you all for making my study and life in UVa exciting and unforgettable.

Table of Contents

List of Figures

List of Tables

Chapter 1
Introduction

1.1. Introduction

Human papillomavirus (HPV), a non-enveloped icosahedron double-stranded DNA virus, is the second leading cause of cancer around the world and is associated with 30-40 types of common skin warts and anogenital disease including cervical cancer and genital warts in both genders [1]. Among 150 species of HPV identified by their genotypes types 18 and 16, which are referred to as high-risk subtypes, cause about 70-80% of cervical cancer cases whereas other types such as 6 and 11 cause benign condylomas. A recent report shows that 2,000,000 deaths related to HPV diseases occur worldwide every year [2]. Currently, the most effective way to prevent the disease is the HPV vaccine. A nine-valent vaccine, Gardasil 9, produced by Merck & Co., Inc. is already been widely used. Although the vaccine was first launched in June 2006, its high cost still limits distribution in developing countries [3] and since a significant portion of the cost comes from downstream processing, improving and understanding of VLP purification is crucial.

HPV virus like particles (VLPs) mimic the HPV's capsid, the outer protein shell. The native HPV capsid consists of 72 protein subunits or capsomeres. The capsomeres contain major L1 protein (~55 kDa) pentamers and minor L2 protein (~75 kDa) pentamers. L1 protein has the intrinsic property of self-assembly into VLPs and L2 protein is believed to facilitate virus DNA encapsulation. It has been shown that HPV VLPs composed of L1 and L2 protein appeared identical in size and shape to the VLPs composed of only L1[4]. **Figure 1** shows the structure of HPV Type 16 composed only of L1 protein obtained by Cryo-EM reconstruction. VLPs are able to self-assemble into capsid structures *in vivo* or *in vitro* at high-ionic-strengths [5]. Recombinant

HPV VLPs with only L1 major capsid proteins have been expressed in different host cells. Eukaryotic expression systems, such as a galactose induced *Saccharomyces cerevisiae,* are most commonly used because of cost-effectiveness and easy adaptability to large-scale production. Most importantly, yeast cells have lower potential for toxin and infectious virus contamination compared to other expression systems such as bacterial or mammalian cells [6]. Recombinant HPV VLPs elicit a strong immune response characterized by expression of high levels of neutralizing antibodies that immunize people from the VLP-derived virus while being non-infectious due to its lack of the viral genome. This mechanism makes VLPs ideal as vaccines.

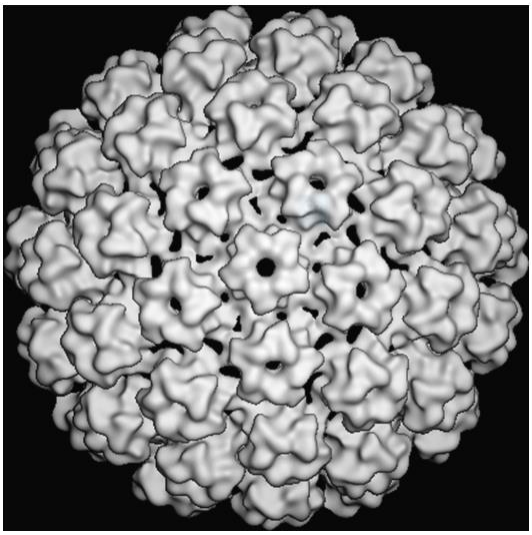

Figure 1 Cryo-EM reconstruction of an HPV16 pseudovirion calculated at 18 Å resolution [7].

Due to the high-value potential of VLPs, many studies dealing with their purification have been published in recent years. Sucrose cushion ultracentrifugation for primary recovery of VLPs has been used at the laboratory scale [8][9][10]. Min-A Park introduced an ammonium sulfate precipitation step which obtains a yield rate up to fifteen times greater than the ultracentrifugation method [6]. However, these methods are expensive and difficult to scale up. Monoliths have been proposed as alternatives for capture due to their larger characteristic pore

sizes that can accommodate VLPs [11]. Technological difficulties currently limit their scale-up. Cation-exchange chromatography is thus used in practice, as a scalable and efficient process, for initial capture of VLPs.

VLPs have a large size, ranging from 60-100 nm in diameter, much larger than protein pharmaceuticals such as monoclonal antibodies. Previous work by Wu has shown that even when resins with large pore size (e.g. POROS 50HS) are used, adsorption of VLP Type 11 is still limited to the resin particle outer surface due to the steric blocking of the resin pores. Thus low binding capacities are observed [11]. The uneven charge distributions caused by their large size is another consideration, not only in determining the isoelectric point but also for the choice of capture adsorbent. While considerable research has been done related to the structure and purification processed for Type 11 and Type 16 VLP [6] [8] [10], less is known about Type 18. Despite the fact that the degree of chemical and structural homology of different types of HPV L1 capsids is high [12], Type 18 is known to exhibit unique process-relevant characteristics.

Figure 2 shows a typical purification process of VLP Type 18. The capture step uses CEX, which is followed by a polishing step with hydroxyapatite chromatography. A particular concern is RNA clearance in the purification of HPV Type 18 VLP. In a typical purification process, RNA from the host cell is digested with an RNase treatment following cell lysis and before flowing into the product capture column. However, it has been observed that relatively high RNA contamination (300 ng/mL) accompany the Type 18 VLP, requiring further processing to attain acceptable RNA clearance.

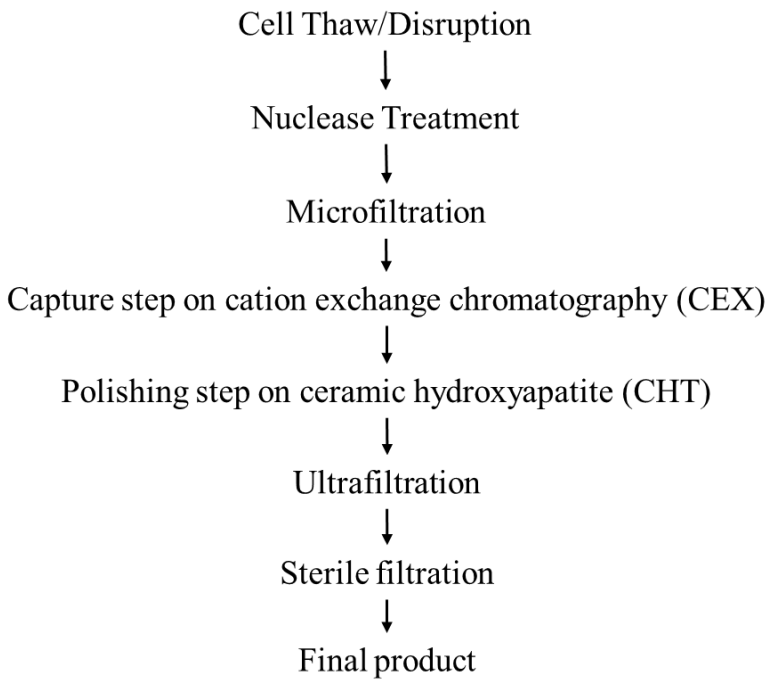

Figure 2 Overview of HPV VLP Type 18 purification process [13].

Several proteins have been shown to be capable of association with RNA [14][15][16]. For example, well characterized RNA-binding proteins have been shown to specifically bind the 3' untranslated regions of mRNAs and other nucleic acid groups [17]. Non-specific binding of nucleic acids to HIV-1 Rev protein has also been shown [18]. This evidence suggests that the observed RNA contamination of Type 18 VLP may be caused by association with RNA. Such association may affect the purification process in different ways. Firstly, in the capture chromatography step, negatively charged RNA may reduce the binding strength of the positively charged VLPs, resulting in complex salt elution patterns of the VLPs that vary with their degree of RNA association. Secondly, in the CHT polishing chromatography step, the possible association of RNA with VLPs could prevent effective removal of RNA or reduce product yield. Clinically, even trace amounts of host cell impurities could potentially cause adverse immunogenic responses in patients. Thus, it is critical to address the binding behavior of RNA to

VLPs and chromatographic adsorbent. Thus, one objective of this work is explore to what extent RNA associates with VLPs and affects purification.

To study the interaction between RNA and VLPs, biolayer interferometry (BLI) is proposed as a tool to measure the association rate constant (k_a) and the dissociation equilibrium constant (K_d). In the past, RNA-protein interactions were characterized using different techniques such as filter-binding assays, electrophoretic mobility shift assays, and structural studies [19] [20]. Although such methods can yield valuable information, they provide little or no quantitative data. The hypothesized RNA-VLP association is likely to be dynamic, and knowing the interaction under different solution conditions is essential for the design of purification process. With BLI, a VLP sensor can be made by adding VLPs on a negatively charged biosensor surface exploiting the strong electrostatic interaction with positively changed VLPs. This method provides a promising way to study the interaction between RNA and VLP without any modification of the VLPs. Alternatively, a RNA sensor can be made by immobilizing biotinylated RNA on a streptavidin coated biosensor surface, taking advantage of extraordinarily high affinity between streptavidin and biotin with an estimated dissociation equilibrium constant of about 10^{-14} M [21].

Understanding the mechanism of polishing chromatography is also necessary to establish the optimum purification condition. Hydroxyapatite (HAP) chromatography was first introduced in 1956 to purify molecules with a high percentage of phosphate groups, such as DNA and RNA [22]. Ceramic hydroxyapatite (CHT) used in this step consists of sintered HAP crystals with formula of $Ca_{10}(PO_4)_6(OH)_2$ [23]. As a result, CHT contains negatively charged phosphate surface sites (P-sites) and positively charged calcium surface sites (C-sites), which provide a cation exchange binding mechanism and a calcium affinity binding mechanism. Basic proteins in their cationic form tend to bind to the P-sites due to electrostatic interactions and are simultaneously repelled

by the C-sites. Thus, binding of these proteins depends on the combined effects of these interactions. Calcium affinity, on the other hand, occurs via interactions between carboxyl groups on the protein surface and the C-sites. The calcium affinity of molecules is 15-60 times stronger than electrostatic repulsive forces. This affinity adsorption has been proven by evaluating the retention of proteins on which carboxyl have been replaced by sulfo groups [24]. Binding is reduced dramatically even though the net charge is unaltered. Adsorption of protein and DNA on CHT has been investigated by many previous studies. Chen et al., for example, concluded that the interaction of small double-stranded DNA fragments with HAP was an electrostatic interaction [25]. Giovannini and Freitag found that different sintering temperatures used in the manufacture of CHT resulted in different surface properties such as the distribution of P-sites and C-sites. Those differences make the different types of CHT exhibit different binding capacity and selectivity [26]. Two commercial CHTs were reported to behave differently by Bio-Rad laboratories [27]. CHT Type I has a higher binding capacity for acidic protein than CHT Type II. CHT Type II has a lower protein binding capacity but gives better resolution for nucleic acids and for certain protein mixture. However, the adsorption behavior of VLP on CHT and the selectivity of RNA with VLP on CHT have not been investigated.

.

Chapter 2
Project Objectives

2.1. Project Objectives

This project has two principal objectives. The first is to characterize RNA-VLP association using BLI. The principle of this technique is illustrated in **Figure 3**. BLI utilizes a fiber optic with two light reflecting layers; a thin top layer with a high refractive index (e.g., n > 1.8) and a thick bottom layer with a refractive index intermediate between the solution and the top layer (e.g., n = 1.5). White light traveling through the fiber optic is partially reflected back by the top layer and partially reflected back by the bottom layer (**Figure 3**(a)). Since the distance traveled by the light reflected by the two layers is different, constructive and destructive interference occurs resulting in the wave form illustrated in **Figure 3**(b). The overall wavelength-dependent intensity of the interference wave is given by [28]:

$$I = I_1 + I_2 + 2\sqrt{I_1 I_2}\, cos\left(\frac{2\pi d}{\lambda}\right) \quad (1)$$

where I is the intensity, I_1 and I_2 are the intensities of two interfering waves, d is the optical path length difference, and λ is the wavelength. If an analyte binds to the bottom layer (**Figure 3**(c)), the wave form shifts since the path length is effectively increased. The binding signal, measured by the wave length shift, is directly related to the thickness of the bound analyte layer.

In order to monitor the interaction between two species by BLI, one of the two species is attached to the fiber optic sensor. Vigorous shaking of the sensor placed in a small well containing the solution with the other species is used to mitigate mass transfer effects. By monitoring the wavelength shift, association of the two species can be detected in real time. In

our case, we can either immobilize RNA and keep VLP in solution or immobilize VLP and keep RNA in solution. The specific work to be conducted involves:

a. Construct immobilized RNA and VLP biosensors;

b. Test the ability to detect RNA-VLP association;

c. Determine binding constants; and

d. Determine the effect of solution composition on RNA-VLP association.

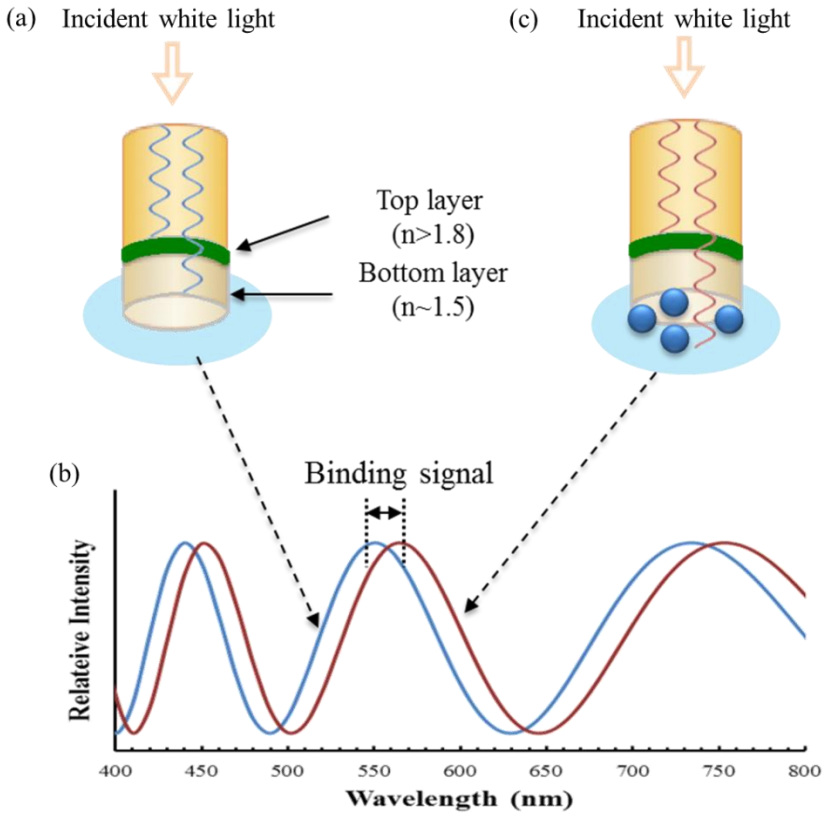

Figure 3 Scheme of biolayer interferometry.

The second objective of this work is to characterize VLP and RNA binding to CHT Type II. As discussed in Chapter 1, CHT is comprised of HAP nanocrystals that are sintered together at various temperatures to form macroporous spherical particles. The CHT II particles used here are

nominally 40 μm in diameter, while the nanocrystals are on the order of 50 to 200 nm. The specific tasks related to this objective are:

a. Characterize the CHT structure in terms of pore size and porosity;
b. Determine the chromatographic separation performance for RNA/VLP mixtures; and
c. Image the distribution of bound RNA and bound VLP within the CHT particles by confocal laser scanning microscopy (CLSM).

Chapter 3
Material and Methods

3.1. Materials

3.1.1. Chemicals

Recombinant HPV VLPs Type 11 and Type 18 (MW ≈ 5,500 kDa) were obtained from Merck & Co., Inc. (Elkton, VA). Frozen samples were thawed at room temperature in a water bath; then 0.015% Polysorbate 80 (Amresco, Solon, OH) was added to increase stability [29]. Finally, aliquots were refrozen at -80°C. The extinction coefficient provided by Merck based on a protein assay is 1.415 mL/(mg of VLP protein×cm) at 280 nm.

Dynamic light scattering (DLS) was used to determine the hydrodynamic radius (r_h) of the VLPs. This method also provides insight as to whether the conformation of VLPs changes or aggregation occurs. DLS analyze were done at 20 °C using a Dynapro Nanostar unit (Wyatt Technology Corporation, CA). All data were analyzed with DYNAMIC 7.1 using a "Cumulant fit" of the autocorrelation function. Solvent refractive index and viscosity were assumed to be 1.34 and 1.03 cP, respectively. A summary of DLS results is given in **Table 1**. **Figure 4** shows the size distribution of the VLPs under different conditions. Although the data show that the particle size distribution is broadened slightly after various processing steps, the mean r_h does not change significantly.

Table 1 Summary of size measurement of VLP particles

Sample	Treatment	r_h (nm)
VLP Type 18	Stock solution	37
VLP Type 18	After buffer exchange to load buffer	34
VLP Type 18	After dye labeling and dye removal	32
VLP Type 18	Collection from elution	32
VLP Type 11	Stock solution	50 [11]

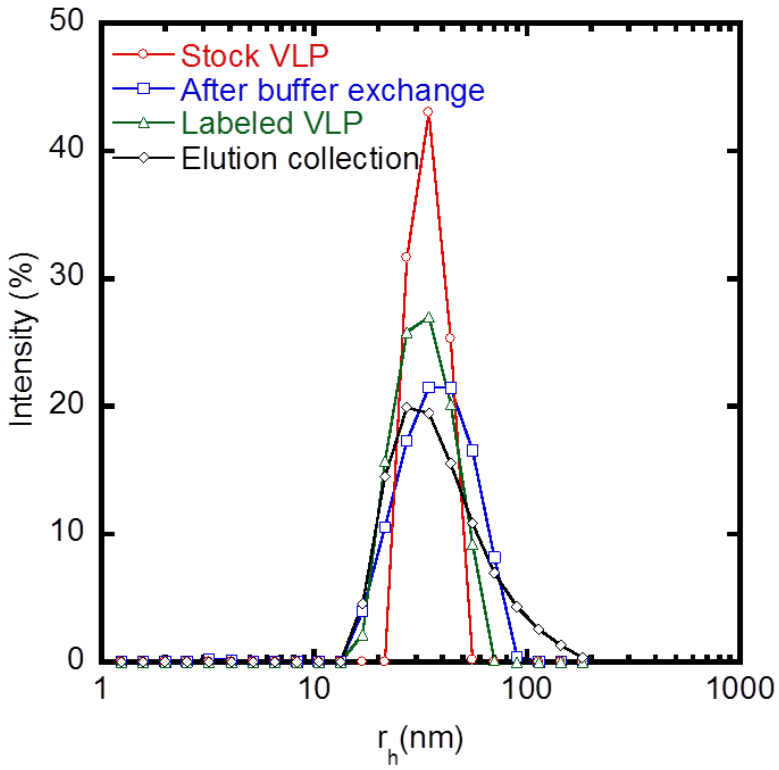

Figure 4 DLS results of VLP Type 18 particles.

RNA from *S. cerevisiae* was obtained from Sigma-Aldrich Co. (St. Louis, Mo). The extinction coefficient of RNA is 25 mL/(mg×cm) at 260 nm as estimated from a gravimetric determination. The molecular mass of the RNA was determined by agarose gel electrophoresis using a transcript

RNA marker (0.28 – 6.6 kb) (Sigma-Aldrich, St. Louis, Mo) as a standard. **Figure 5** shows the electrophoresis results. A relatively broad band is seen corresponding to a heterogeneous size distribution averaging around 500 bases. The corresponding average molecular weight is estimated to be 170 kDa based on an average nucleotide molecular mass of 340 g/mol. While we cannot be absolutely sure, it is likely that the RNA in the actual VLP purification process would also be small in size, since RNase is used to digest large RNA.

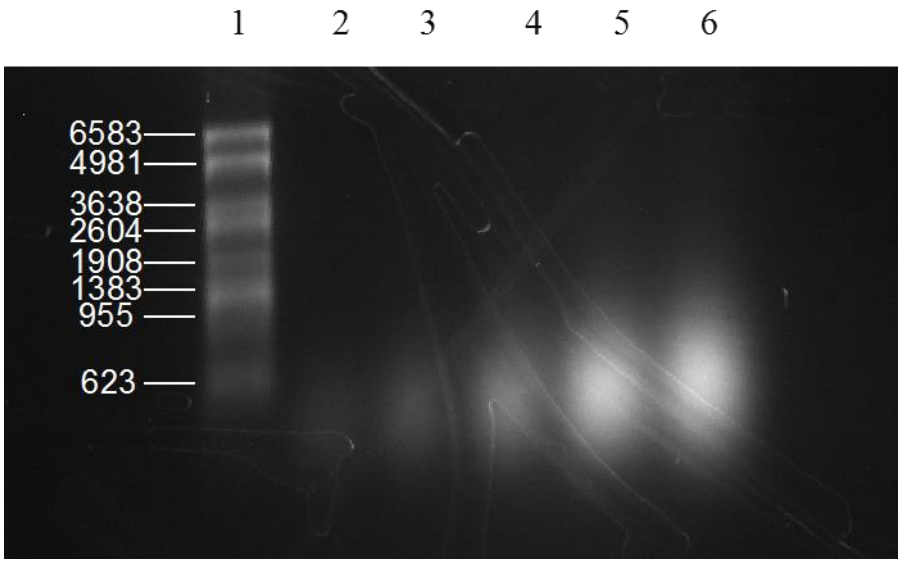

Figure 5 Electrophoresis analysis of RNA sample. RNA was denatured with glyoxal and DMSO and electrophoresed on a 1% agarose gel. Lane 1, RNA ladder, 2 to 6, serial diluted RNA from 50 ng/mL to 800 ng/mL.

A purified monoclonal antibody (mAb), used as a model protein (MW~150 kDa, pI~7.8), was obtained from MedImmune LLC (Gaithersburg, MD). Its extinction coefficient at 280 nm is 1.49 mL/(mg×cm) as provided by MedImmune. All other chemicals were purchased from Fisher Scientific (Pittsburgh, PA).

3.1.2. Stationary Phase

The CHT adsorbent used in this work is Type II (CHT II) and was obtained from Bio-Rad Laboratories (Hercules, CA). CHT is in the form of spherical macroporous particles. The nominal particle size is 40 μm. The adsorbent was flow-packed in a 1 cm diameter × 10 cm long Tricorn 10/100 column (GE Healthcare, Piscataway, NJ) at 5 mL/min to a final bed volume of approximately 6.75 mL.

3.2. Methods

3.2.1. Biolayer Interferometry

VLP-RNA association was studied with either a BLItz system or an Octet Red96 instrument both from Pall ForteBio Inc. (Menlo Park, CA). The only difference between these two is that the Octet uses eight probes in parallel while the BLItz uses one. All BLI experiments were conducted at room temperature in a pH 7 phosphate buffer with vibration set at 1500 rpm. Each biosensor was hydrated with the loading buffer (250 mM NaCl and 5 mM Na_2HPO_4) for at least 600 s immediately prior to use. The microtubes used for BLItz or microplates used for Octet were filled with 200 μl solution. All measurements were performed in triplicate and each measurement was performed on a fresh tip. The BLItz data was fitted by BLItz Pro system and Octet Data was fitted by Data Analysis system both with 1:1 model.

Amine reactive (AR2G) probes were obtained from Pall ForteBio Inc. and were used for immobilizing the VLPs. The surface of these probes is covered with carboxyl groups which are negatively charged and interact favorably with positively-charged proteins. We expect the AR2G surface to bind the VLPs (which are positively charged) strongly provided that the ionic strength of the solution is not too high. For example, Wu found that HPV VLPs were strongly bound to the negatively charged resin POROS HS at salt concentration as high as 500 mM [11].

Experiments with these VLP biosensors were done as follows. Each biosensor was dipped in the loading buffer for 30 s to establish a stable baseline and then dipped in a 5 nM VLP solution for 120 s. The probe was then dipped into the AR2G binding buffer (1% BSA in 250 mM NaCl and 5 mM Na_2HPO_4) again without VLP to establish a baseline for the next step. Finally, the probes were dipped in to serially diluted RNA samples to measure the RNA association kinetic for 200 s and again in the same AR2G binding buffer without RNA to measure the dissociation kinetics for 200 s.

Streptavidin (SA) probes were also obtained from Pall ForteBio Inc. These probes contain immobilized SA which can be used to couple biotinylated molecules. In our case, these probes were functionalized with biotinylated RNA. For this purpose, RNA was biotinylated using the biotinamidohexanoic acid hydrazide based on the selective periodate-mediated oxidation of the RNA 3'terminal ribose *cis*-diol [30]. RNA was first incubated in 40 mM KIO_4 for 1 h at room temperature in the dark. Then the reaction was stopped by adding 50% ethylene glycol, 3M NaOAc (pH 5.2) and 96% ethanol to precipitate RNA. RNA was recovered by centrifugation at 13,000 rpm for 15 min. The pellet was washed by 70% ethanol and dry by air. Then it was dissolved in 10 mM biotinamidohexanoic acid hydrazide and incubated for 2 h at 37°C. The final step was stabilized the biotinylated RNA by borohydride reduction using 0.2 M $NaBH_4$ and 1 M Tris-HCl (pH 8.2) on ice in the dark for 30 min. A PD 10 desalting column (GE Healthcare, Piscataway, NJ) was used to remove the unreactive dye and other salts.

Experiments with the RNA biosensors were done as follows. Like the previous experiment, each biosensor was dipped in the loading buffer (250 mM NaCl and 5 mM Na_2HPO_4) for 100 s to establish a stable baseline and then dipped in a 10 nM RNA solution for 100 s. Then these probes were passivated with 0.5X casein blocking buffer from Sigma-Aldrich Co. (St. Louis, Mo) and

0.02% biotin in loading buffer for 200 s. The probes were then dipped into the SA binding buffer without VLP to establish a baseline. SA binding buffer is 0.01% Tween-20 (polysorbate 20) in 250 mM NaCl with 5, 30, 50, 100 mM Na_2HPO_4 respectively. Finally, the probes were dipped into serially diluted VLP samples to measure the VLP association kinetics for 1000 s and again in SA binding buffer without VLP to measure the dissociation kinetics for 1000 s.

In order to extract rate and equilibrium constants, the sensorgrams obtained for the AR2G-VLP probes were processed with a second-order 1-1 binding model as shown below [31]. The model assumes that association between the species in the solution (A) and the surface-bound species (B) occurs according to:

$$\mathrm{A} + \mathrm{B} \leftrightharpoons \mathrm{AB} \tag{2}$$

with the association rate described by:

$$\frac{d[\mathrm{AB}]}{dt} = k_a[\mathrm{A}][\mathrm{B}] - k_d[\mathrm{AB}] \tag{3}$$

where brackets denote molar concentrations.

Assuming that the signal R is proportional to [AB], integration of eq. (3) with initial condition $R(0) = 0$ and assuming that [A] is constant yields:

$$R = \frac{R_{max}[\mathrm{A}]k_a}{k_a[\mathrm{A}] + k_d}\{1 - \exp[-(k_a[\mathrm{A}] + k_d)t]\} \tag{4}$$

where R_{max} is proportional to the maximum value of [AB].

A more complicated relationship is obtained if the concentration of [A] resulting from binding is accounted for. In this case, the parameter α ($\mathrm{nm} \times \mathrm{mm}^2/\mathrm{ng}$) is introduce to convert the signal R into a concentration. Accordingly, the concentration of A is related to its initial value $[\mathrm{A}]_0$ by:

$$[\mathrm{A}] = [\mathrm{A}]_0 - \frac{SR}{\alpha M_A V} \tag{5}$$

Additionally,

$$[\mathrm{B}] = [\mathrm{B}]_0 \left(1 - \frac{R}{R_{max}}\right) \tag{6}$$

$$[\mathrm{AB}] = \frac{[\mathrm{B}]_0 R}{R_{max}} \tag{7}$$

where S is the probe surface area (m^2), V is solution volume of the ligate (L), $M_A$is the molecular weight of A.

Combining eqs. (3) and (5)(6)(7) gives,

$$\frac{dR}{dt} = k_a \beta \left[R^2 - \left(\frac{[\mathrm{A}]_0}{\beta} + R_{max} + \frac{k_d}{\beta k_a}\right) R + \frac{[\mathrm{A}]_0}{\beta} R_{max}\right] \tag{8}$$

where $\beta = S/\alpha M_A V$. Solving this equation with the condition $R(0) = 0$ gives:

$$R = q\left(1 - \frac{p - q}{pE(t) - q}\right) \tag{9}$$

where $E(t) = \exp[k_a \beta (p - q)t]$, and p and q are the roots of the quadratic equation:

$$R^2 - \left(\frac{[\mathrm{A}]_0}{\beta} + R_{max} + \frac{k_d}{\beta k_a}\right) R + \frac{[\mathrm{A}]_0}{\beta} R_{max} = 0 \tag{10}$$

A different result is obtained for the dissociation process when $R(0) = \mathrm{R}_0$. R_0 is the signal in the end of the association. In this case,

$$[\mathrm{A}] = \frac{-S(R - R_0)}{\alpha M_A V} = \beta (R - R_0) \tag{11}$$

Substituting eq. (3) we obtained :

$$\frac{dR}{dt} = k_a\beta\left[R^2 - \left(R_0 + R_{max} + \frac{k_d}{\beta k_a}\right)R + R_0 R_{max}\right] \quad (12)$$

which upon integration gives:

$$R = \frac{(p'q' - q'R_0)E(t) - p'q' + p'R_0}{(p' - R_0)E(t) - q' + R_0} \quad (13)$$

where $E(t) = \exp[k_a\beta(p' - q')t]$, p' and q' are calculated in the same way as p and q.

Values of $k_a$and k_d obtained with the BLI software and those obtained with fitting eqs.(9) and (13) directly to the sensorgrams were compared. This fitting was done by importing the original data into Excel and using the Excel function "Solver" to determine the values of k_a, k_d and R_{max} that minimize the sum of residual squares between model and data. A comparison of the results is given in Section 4.1.

3.2.2. Chromatographic and Adsorption Experiments

3.2.2.1. Characterization of CHT Pore Size and Porosity

The pore size and porosity of the CHT adsorbent were obtained by inverse size exclusion chromatography (iSEC) using polyethylene glycol (PEG) probes with molecular weight between 300 and 35,000 Da. The iSEC experiments were conducted with 10 µL injections of 5 g PEG/L in 250 mM NaCl, 5 mM Na_2HPO_4 at pH 7 with a Waters HPLC system and a Waters 2414 refractive index detector (Waters, Milford, MA)

The elution volume at the peak maximum of the PEG response peaks,V_R, was used to calculate the distribution coefficient as follows:

$$K_D = \frac{\frac{V_R}{V_c} - \varepsilon}{1 - \varepsilon} \tag{14}$$

where V_c is the column volume and ε is the exraparticle porosity. In turn, ε was obtained by determining the column pressure drop as a function of flow rate and comparing the results to the Carman-Kozeny equation:

$$\Delta P = 150\ \frac{(1-\varepsilon)^2}{\varepsilon^3}\eta\frac{Lu}{{d_p}^2} \tag{15}$$

where η is the mobile phase viscosity, u the superficial velocity, L the column length, and d_p the particle diameter. Finally, mean pore radius (r_{pore}) and intraparticle porosity (ε_p) were obtained by comparing the experimentally determined K_D values based on eq. (14) with the following eq. (16) which assumes cylindrical pores with uniform radius r_{pore} [32]:

$$K_D = \varepsilon_p\left(1 - \frac{r_h}{r_{pore}}\right)^2 \tag{16}$$

The total intraparticle porosity is calculated based on the intraparticle porosity and extraparticle porosity as follows:

$$\varepsilon_{total} = \varepsilon + (1-\varepsilon)\varepsilon_p \tag{17}$$

3.2.2.2. Transmission Electron Microscopy

Transmission electron microscopy (TEM) was used to observe the internal structure of CHT particles. CHT samples for TEM were prepared by immersing the particles in the acrylic resin LRWhite (London Resin Company, London, UK) and incubating them at 45°C overnight as discussed in reference [33][34]. The solid samples were then sectioned into 80 nm sections by ultramicrotome and viewed with a JEOL JEM-1230 transmission electron microscope.

3.2.2.3. Chromatographic Experiments

A 20CV linear phosphate gradient from 5 to 200 mM Na_2HPO_4 with 250 mM NaCl was used to separate VLPs from RNA. VLP (0.25 mg/mL) and RNA samples (0.8 mg/mL) were both prepared in loading buffer (250 mM NaCl, 5 mM Na_2HPO_4). All experiments were at a flow rate of 1 mL/min using an ÄKTA Pure 25 unit from GE Healthcare (Piscataway, NJ) controlled by UNICORN software version 7.0. The experiments were conducted with 500 μL injections and were run at a mobile phase velocity of 76 cm/h. All the buffers were at pH 7 and all the experiments were conducted at room temperature.

3.2.2.4. Adsorption Isotherms

Adsorption isotherms were obtained by adding known weights of hydrated CHT particles into RNA solution of different initial concentration in 1.5 mL plastic tubes. All buffers were treated with diethylpyrocarbonate (DEPC) to remove any RNase. The ratio of particles to solution volumes was estimated to yield a 50% drop from the initial RNA concentration. The tubes were sealed and slowly rotated end-over-end on a wheel at room temperature. After 24 h, the CHT particles were settled by centrifugation at 5,000 rpm for 5 min and the supernatant RNA concentration was determined with a Nanodrop 2000c UV–Vis spectrophotometer (Thermo Scientific, Wilmington, DE) at 260 nm. Material balances were used to calculated the adsorbed RNA.

The density of hydrated CHT particles was measured with a pycnometer. For this purpose, hydrated CHT particles were prepared as follows. First, particles were immersed in the loading buffer and then drained by centrifuging them at 2,000 rpm for 14 min in microcentrifuge filters to remove the liquid from the extraparticle space. Then the weight of hydrated particles was measure in pycnometer. The volume was calculated by replacing a water-filled pycnometer with

hydrated particles and converting the displaced water volume into the hydrated CHT particle volume. The density obtained from the experimental measurement is 1.44 g/mL. This value can be compared with that obtained with the following equation:

$$\rho = \rho_{water}\varepsilon_p + (1 - \varepsilon_p)\rho_{HAP} \tag{18}$$

where the theoretical density of HAP (ρ_{HAP}), is 3.1 g/mL [35]. The value of ρ obtained from this eq. (18) is 1.60 g/mL based on ε_p obtained from the iSEC experiments.

Association of RNA on CHT can be described quantitatively by the Langmuir isotherm model:

$$q = \frac{q_m KC}{1 + KC} \tag{19}$$

where q is the adsorbed concentration, q_m is the maximum adsorption capacity, C is the concentration in the solution, and K is the binding equilibrium constant.

3.2.2.5. Confocal Laser Scanning Microscopy

Confocal laser scanning microscopy (CLSM) was used to observe the intraparticle distribution of RNA and VLPs during transient adsorption. Images were obtained with a Zeiss LSM 510 microscope with Plan-Neofluar 40X/1.3 NA Oil objective (Carl Zeiss MicroImaging, LLC, Thornwood, NY). In order to allow simultaneous observation of the two species, the VLPs were labeled with Rhodamine Red™-X dye while RNA was labeled with Alexa Fluor 488 using a ULYSIS nucleic acid labeling kit both from Molecular Probe (Carlsbad, CA). A 561 nm diode-pumped solid state laser and a 488 nm argon gas laser were used for imaging VLP and RNA, respectively.

Conjugation with the dyes was done as follows. VLP was incubated with Rodamine Red X in 500 mM $NaHCO_3$, pH 8.5 with a dye to protein molar ratio of 1:1 for VLP based on the L1 protein for 30 min at room temperature in the dark. This dye reacts with amine residues that are partially deprotonated. A PD 10 desalting column (GE Healthcare, Piscataway, NJ) was used to remove the unreacted dye after labeling.

The RNA was labeled using a ULYSIS labeling kit (Invitrogen, Carlsbad, CA) which utilizes a platinum dye complex that forms a stable adduct with N7 position of guanine and adenine bases in RNA. The Alexa Fluor 488 ULS reagent was dissolved in 100 μL dimethyl sulfoxide (DMSO) and vortex until no particulate matter remained. 20 μL RNA (50 mg/mL) was labelled by precipitating RNA using 2 μL 3 M sodium acetate (pH 5.2), 40 μL absolute ethanol for 30 min at -80°C, and centrifugation for 15 min at 12,000 rpm. The supernatant was discarded and the pellet was re-suspended with 20 μL labeling buffer. To facilitate labeling, RNA was denatured by heating at 95°C for 5 min and then snapping cooling on ice. 1 μL Alexa Fluor 488 was added to the RNA solution and the sample was incubated at 90°C for 10 min. The reaction was stopped by immersing the sample into an ice bath. Unreacted dye and other salts were removed using a Micro Bio-Spin 30 chromatography column (Bio-Rad, Hercules, CA) at 5,000 rpm for 4 min.

Batch CLSM experiments were done by mixing the labeled VLP and/or RNA with an amount of resin estimated to yield only a 10% drop of sample concentration. Mixing was provided by rotating the tubes end-over-end at 30 rpm. At various times, CHT samples were pipetted out and centrifuged at 13,000 rpm for 30 s to separate the particles from the supernatant using Spin-X microfiltration tubes (Corning Incorporated, Corning, NY). Since the refractive index of CHT backbone is very high, prior to imaging, the particles were immersed in benzyl alcohol (n = 1.54)

or 50% sucrose (n = 1.42) to reduce the refractive index difference between the CHT crystals and the solution [36].

The degree of labeling (DoL), defined on the average ratio of dye to protein in the conjugate was calculated as follows:

$$\mathrm{DoL} = \frac{C_{dye}}{C_{protein}} \tag{20}$$

$$C_{protein} = \frac{A_{280} - CF_{dye}A_{\lambda_{max}}^{Dye}}{\varepsilon_{280}^{Protein} \times l} \tag{21}$$

$$C_{dye} = \frac{A_{\lambda_{max}}^{Dye}}{\varepsilon_{max}^{Dye} \times l} \tag{22}$$

Both VLP and RNA concentrations were calculated based on Beer's law at 280 and 260 nm respectively. The absorbance due to the dye at 280 nm is subtracted using a correction factor (*CF*) given in **Table 2**. The emission and excitation wavelengths as well as extinction coefficients of the dyes are also listed in **Table 2**.

Table 2 Spectral characteristics of the fluorescent dyes used in this work

Dye	λ_{em} (nm)	λ_{ex} (nm)	ε_{dye} ($\mathrm{cm^{-1}M^{-1}}$)	*CF*
Alexa Fluor 488*	492	520	62,000	0.30
Rhodamine Red*	570	590	120,000	0.17
SYTO RNASelect*	490	530	NA	NA

* Data from supplier

3.2.2.6. SYTO Labeling of RNA

SYTO RNASelect green fluorescent cell stain (Invitrogen Corporation, Carlsbad, CA) is a cell-permeant nucleic acid stain that is selective for RNA. As it does not require a hash processing for labeling, this commercial dye was used to stain the VLP sample. RNASelect green stain was dissolved in PBS to make a 500 nM solution. All labeling materials were used immediately after preparation to prevent precipitation. The selective experiments were done by measuring the fluorescence of the pure control proteins or the VLP samples with SYTO RNASelect reagent mixture. The absorbance and the emission wavelength are listed in **Table 2**. Fluorescence intensity was detected with BioTek's Synergy4 fluorescence microplate reader (BioTek, VT). The CLSM experiments were done by incubating VLP with CHT for 20 min at room temperature in 250 mM NaCl , 5 mM NA_2HPO_4, pH 7 buffer. After incubation, CHT was centrifuged at 13,000 rpm for 30 s to remove the extra dye and protein. Finally, CHT particles were washed four times with PBS (5 min per wash) before observation. The observations were done in 50% sucrose solution.

Chapter 4
Results and Discussion

4.1. Binding Affinity Assay

To determine the VLP-RNA association and quantify the affinity of interaction, two types of biosensors were used: an immobilized VLP biosensor and an immobilized RNA biosensor. Experiments were done with both VLP Type 18 and VLP Type 11. Since in practice, RNA association was reported as a potential problem only for Type 18, Type 11 was used as a control.

Figure 6 shows the sensorgrams obtained with the BLItz system for the immobilized VLP sensors. The binding signals of VLP onto the AR2G sensors reached 2.0 (± 0.2) nm consistently (Step II). After binding the VLP to the biosensor, the signal stabilized (Step III). After immersing the probe in RNA solution, the signal decreased as a reason of RNA binding (Step IV). Generally in BLI, binding results in an increasing signal. However, because of the pre-bound VLP, RNA binding signal decrease. A similar behavior has been reported in the literature for lipoparticles bound to the sensors [37]. In these cases, the signal can be flipped in order to be able to fit the model. A monoclonal antibody was used as a negative control immobilized on the biosensor. In this case, no RNA binding was detected (results not shown) so a specific association was confirmed. **Figure 7** shows the resulting R_{max} values and the corresponding standard deviation based on triplicate experiments for association between VLP Type 18 and Type 11 with RNA. One potential risk of VLPs experiments is related to the conformation change of VLPs during detection especially under 1,500 rpm vibration condition. However, this good reproducibility of individual assays indicated this was not a concern. This result also demonstrates the repeatability

of BLI system. All the binding signals of VLP Type 18 are higher than Type 11 which proved that more RNA associated with VLP Type 18.

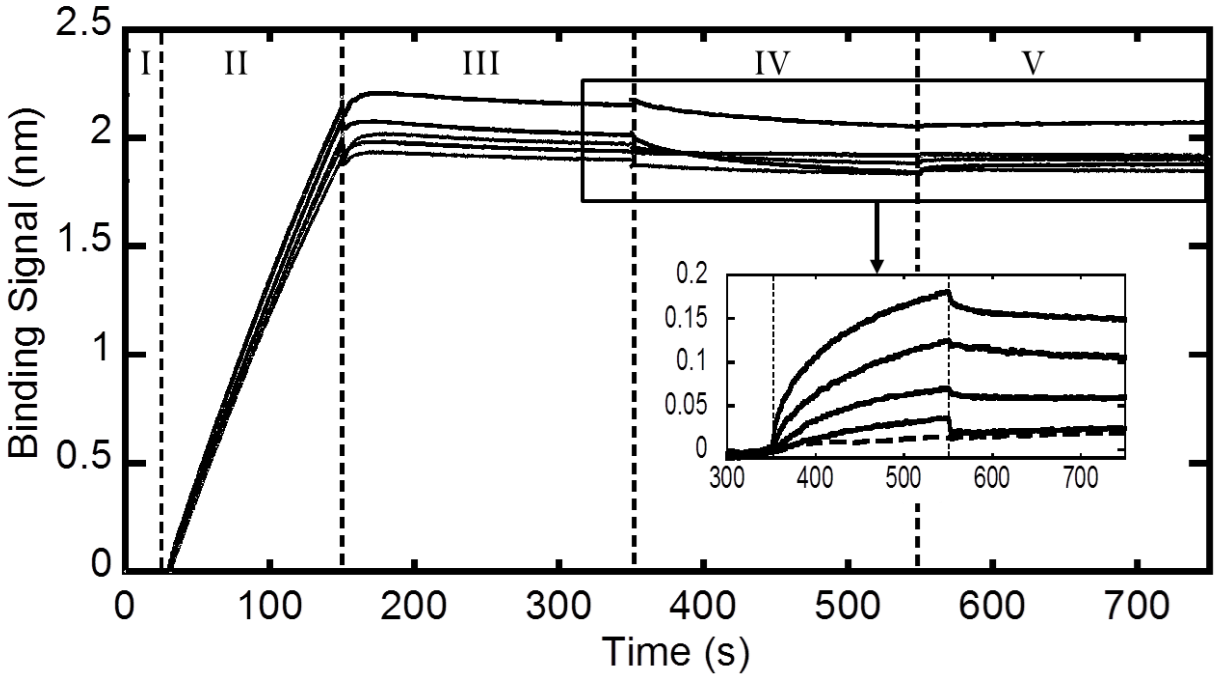

Figure 6 BLI sensorgrams of RNA associated to VLP Type 18 immobilized probes on BLItz. In this experiment, loading buffer is 250 mM NaCl and 5 mM Na_2HPO_4 and AR2G binding buffer is 1% BSA in loading buffer. Step I. Baseline in loading buffer (30 s). Step II. VLP binding to probe in loading buffer (120 s). Step III. Baseline in binding buffer (200 s). Step IV Association with serially diluted RNA samples in binding buffer (200 s) Step V. Dissociation in binding buffer (200 s).The inset shows the flipped association and dissociation signals adjusted to the baseline at the end of step III. The dashed line in the inset shows a control run without RNA.

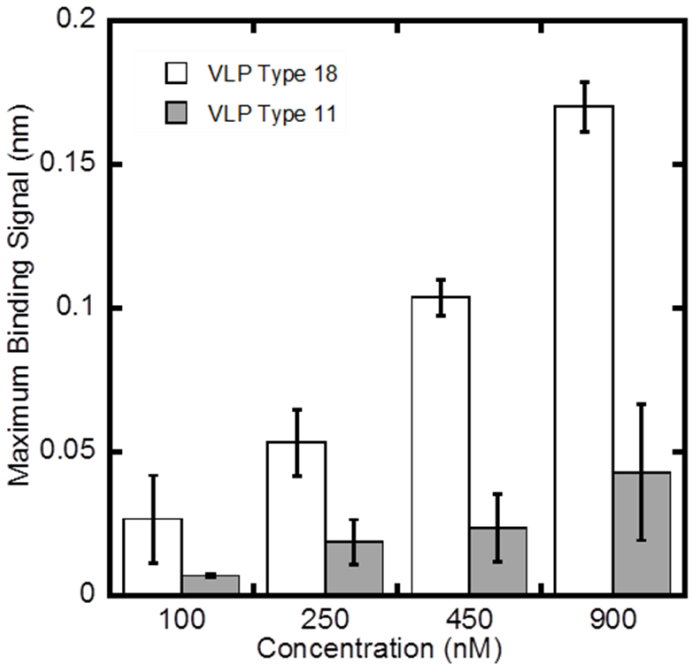

Figure 7 Bars represent the mean R_{max} values determined from BLI experiments with VLP Type 18/11 with 100, 250, 450, 900 nM RNA. Error bars show the standard deviation for triplicate experiments.

Figure 8 shows the sensorgrams obtained with serially diluted RNA solutions with VLP Type 18 (**Figure 8**a) and Type 11 (**Figure 8**b) sensors. The slopes of the dissociation curves are shallow and the decays of the signal are approximately 1/10 of the maximum responses at the end of dissociations indicating that the association is very strong. Incomplete dissociation was observed even after 1000 s (results not shown) demonstrating that association of RNA with VLP is quite stable. **Table 3** gives the kinetic and affinity constants fitted by the BLI software and using Excel according to the 1:1 binding model described in Section 3.2.1. Both the software and Excel implemented model excellently fits to the data, as evidenced by the overlay of the simulated curve and the experimental curves shown in **Figure 8**. The two sets of fitting parameters also show high consistency. The kinetic constant data show that VLP 18-RNA interactions are marked by a fast association rate which is ten time larger than the one from VLP 11-RNA,

resulting in a high affinity constant. These results explain why high RNA contamination was seen with VLP Type 18 but not with Type 11.

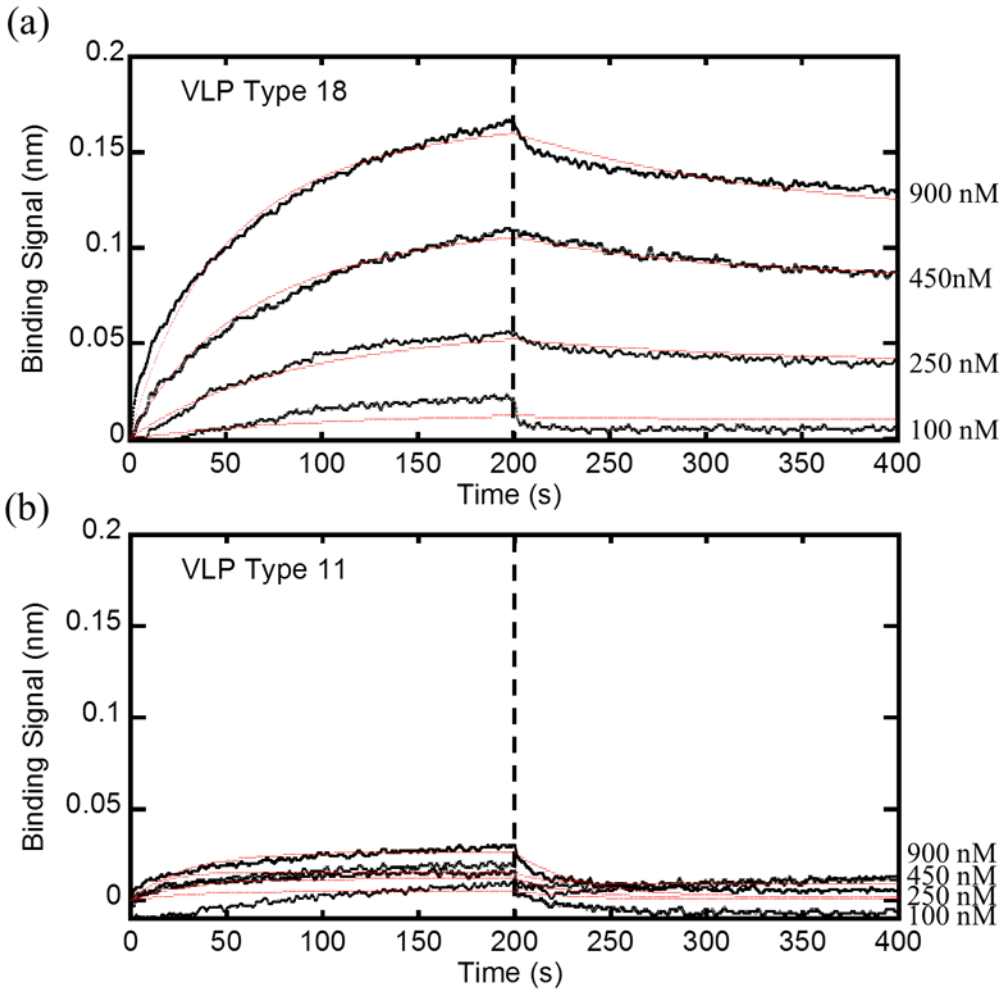

Figure 8 Sensorgrams of RNA association and dissociation to VLP Type 18(a) and VLP Type 11(b) immobilized probes. Time scales were adjusted to zero at the beginning of association. RNA concentrations are 100, 250, 450, 900 nM. Raw data curves for association and dissociation are shown in black lines and software fitted curves are shown in red. The baseline signal in binding buffer was subtracted from each actual signal.

Table 3 Kinetic and affinity constants of RNA binding to VLP Type18 and Type11 immobilized on AR2G sensors fitted with the BLItz software and with Excel based on the second-order 1:1 binding model at 250 mM NaCl and 5 mM Na_2HPO_4.

Protein	Method	$K_d(\mathbf{nM})$	$k_a(\mathbf{M^{-1}s^{-1}})$	$k_d(\mathbf{s^{-1}})$
VLP Type 11	Software fit	3880 ± 272	7.59×10^3	1.16×10^{-2}
	Excel fit	2752 ± 120	4.19×10^3	2.80×10^{-3}
VLP Type 18	Software fit	77.4 ± 4.3	2.05×10^4	1.58×10^{-3}
	Excel fit	84.0 ± 0.1	2.09×10^4	1.34×10^{-3}

To further investigate the effect of buffer composition on the association of RNA-VLP, four different concentrations of dibasic sodium phosphate were tested. With the previous method (**Figure 7**), the most favorable binding still provides a small signal (0.16 nm) due to the small size of RNA. This low response will directly influence the accuracy and the fitting results as the buffer composition changed. Besides, the immobilization of VLP also depends on the buffer ionic strength. Thus, a new experimental setup is necessary to amplify the binding signals. SA-biotin interaction, a robust non-covalent biointeraction, was introduced here to change the binding order. **Figure 9** shows representative kinetic sensorgrams obtained with the Octet system. This time, RNA was biotinylated and immobilized on the SA sensor. The maximal signal shift reaches 1 nm during association. Another concern is related to nonspecific binding on the sensor surface or the unreacted SA. High NSB was observed initially with the previous AR2G binding buffer, which contains 1% BSA. Previous studies showed that casein blocking buffer worked very well for eliminating NSB in enzyme-linked immunosorbent assay (ELISA) [38]. Thus, in order to determine the best passivation buffer, three candidates, including BSA, biotin and casein blocking buffer, with different dilutions and combinations were tested in the preliminary

experiments. In the end, final passivation solution was phosphate buffer with 0.5X casein blocking buffer and 0.02% biotin. Additionally, Tween-20, a non-ionic surfactant, was added to the SA binding buffer to prevent surface adsorption during association and dissociation. The negative control results seen in **Figure 9** shows that the passivation step successfully suppresses the NSB.

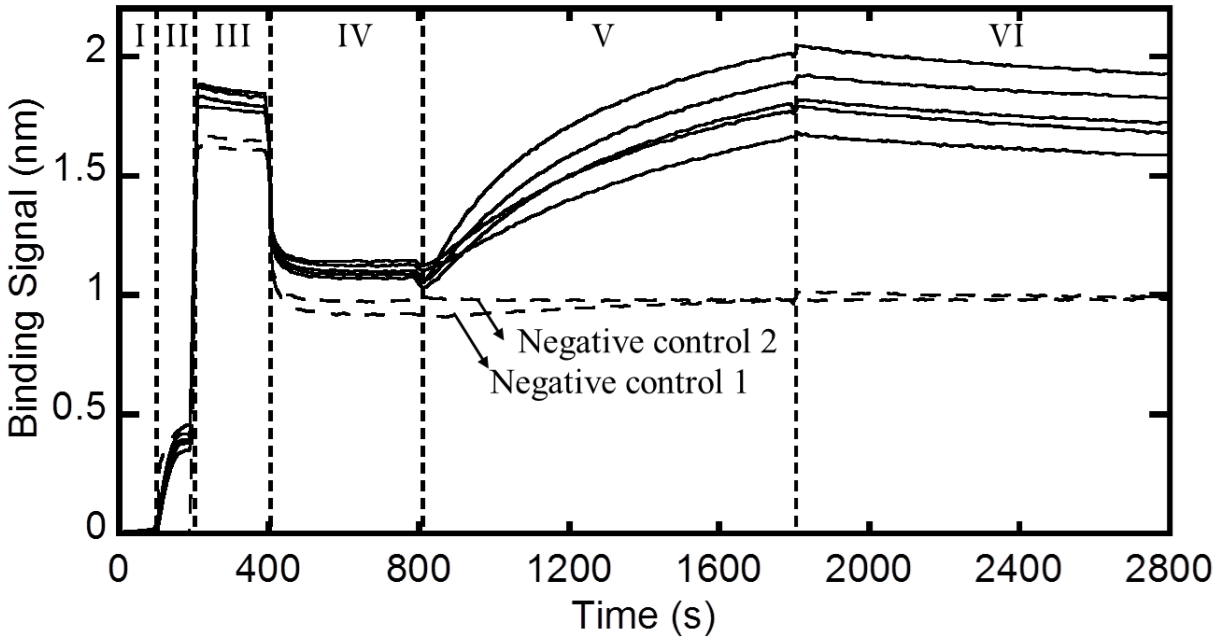

Figure 9 BLI sensorgrams of VLP association with biotinylated RNA immobilized probes on Octet system. In this experiment, loading buffer is 250 mM NaCl and 5 mM Na_2HPO_4, passivation buffer is 0.02% biotin, 0.5X Casein blocking buffer in loading buffer. SA Binding buffer is 0.01% Tween-20 in 250 mM NaCl with 5 mM Na_2HPO_4 in this case. Step I. Baseline in loading buffer (100 s). Step II. Biotinylated RNA binding to probes in loading buffer (100 s). Step III. Biosensor passivation in passivation buffer (200 s). Step IV. Baseline in SA binding buffer (400 s). Step V. Association with serially diluted VLP in SA binding buffer (1000 s). Step VI. Dissociation with SA binding buffer (1000 s). The dashed lines are control runs. Negative control 1is a run without biotinylated RNA and negative control 2 is a run without the VLP.

Figure 10 compares the association of RNA and VLP under different Na_2HPO_4 concentrations. The maximum responses decrease as the Na_2HPO_4 concentration increases indicating that less VLP associates with RNA. **Table 4** gives individual kinetic and affinity constants fitted by the software. The increasing values of the dissociation equilibrium constant with increasing

phosphate demonstrate that the binding affinity is weakened by Na_2HPO_4. As seen in this Table, K_d increases approximately 1000-fold from 5 mM ($K_d = 6.9 \pm 0.2$ nM) to 100 mM Na_2HPO_4 ($K_d = 4920 \pm 261$ nM). An important conclusion derived by comparing the results obtained for VLP and RNA sensors is that the kinetic and affinity constants are not the same for the two cases. This is consistent with the results obtained by surface plasmon resonance (SPR), a technique that shares some similarity with BLI [39]. The equation (8) shows that fitting is highly dependent on the analyte concentration in the solution. That is why high concentration of RNA gives higher dissociation constants. Apparently, VLP-sensor binding is not 1:1 since the large surface area of VLP provides several binding sites of RNA. Thus, K_d value obtained from the RNA-sensor ($K_d = 6.9 \pm 0.2$ nM) will be more trustworthy.

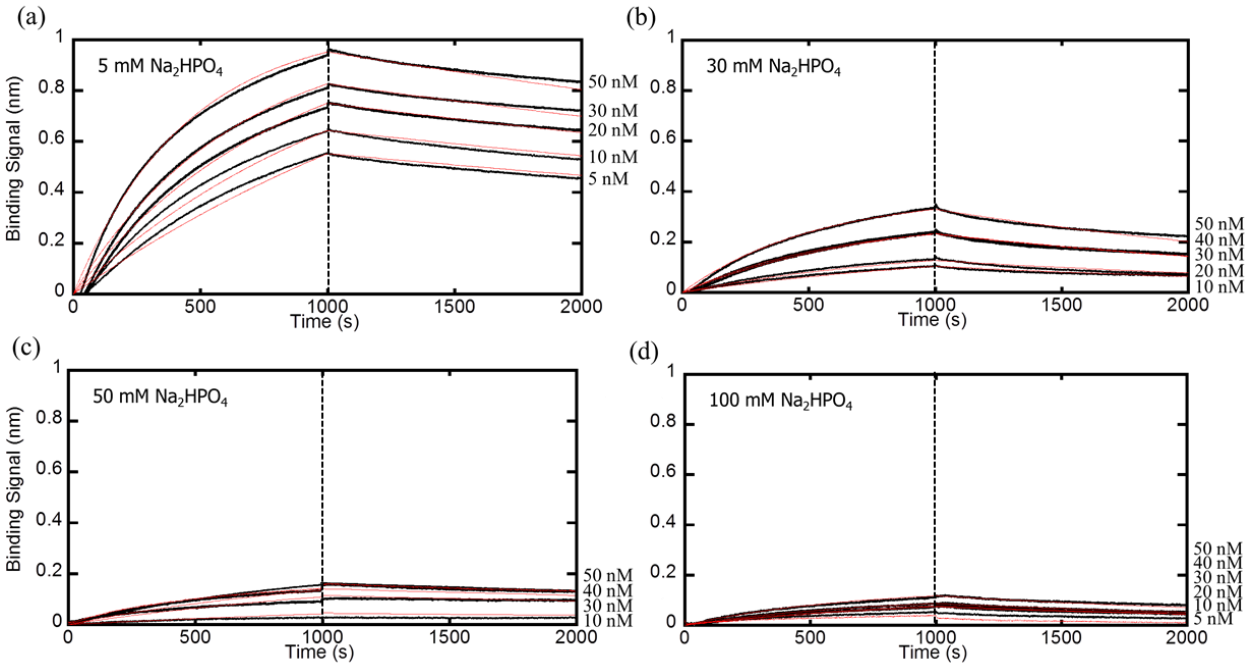

Figure 10 Sensorgrams of VLP association and dissociation to immobilized RNA probes at different phosphate concentrations. All the experiments were done following the same procedures described in **Figure 8** except that different phosphate concentrations were used. Phosphate concentrations were 5 mM Na_2HPO_4 (a), 30 mM Na_2HPO_4 (b), 50 mM Na_2HPO_4 (c), 100 mM Na_2HPO_4 (d) respectively. Time scales were adjusted to zero at the beginning of association. Serially diluted VLP concentrations were labeled on the right. Raw data curves for association and dissociation are shown in black lines and software fitted curves are shown in red. A baseline signal in binding buffer was subtracted from each actual signal.

Table 4 Kinetic and affinity constants of VLP Type 18 binding to biotinylated RNA-immobilized SA sensors at different Na_2HPO_4 concentrations.

Na_2HPO_4 concentration	K_d**(nM)**	$k_a(\mathbf{M^{-1}s^{-1}})$	$k_d(\mathbf{s^{-1}})$
5 mM	6.9 ± 0.2	3.76×10^4	1.97×10^{-4}
30 mM	11.9 ± 0.4	2.25×10^4	2.14×10^{-4}
50 mM	458 ± 15	1.38×10^3	4.61×10^{-4}
100 mM	4920 ± 261	2.38×10^2	1.03×10^{-3}

4.2. Chromatographic and Adsorption Experiments

4.2.1. Adsorbent Properties

Figure 11 shows representative TEM images of CHT particles. In both images, the gray areas are the embeding LRWhite resin while the dark features are the CHT crystals. The white spots are defects due to the sectioning and/or incomplete infiltration of the embedding resin. At lower magnification (**Figure 11**a), it can be seen that the hydroxyapatite crystals are distributed fairly evenly through the particle. At higher magnification (**Figure 11**b), the crystals are easily discernible with a diameter of 100-300 nm, sintered together to form the pores that are approximately 50-200 nm in size.

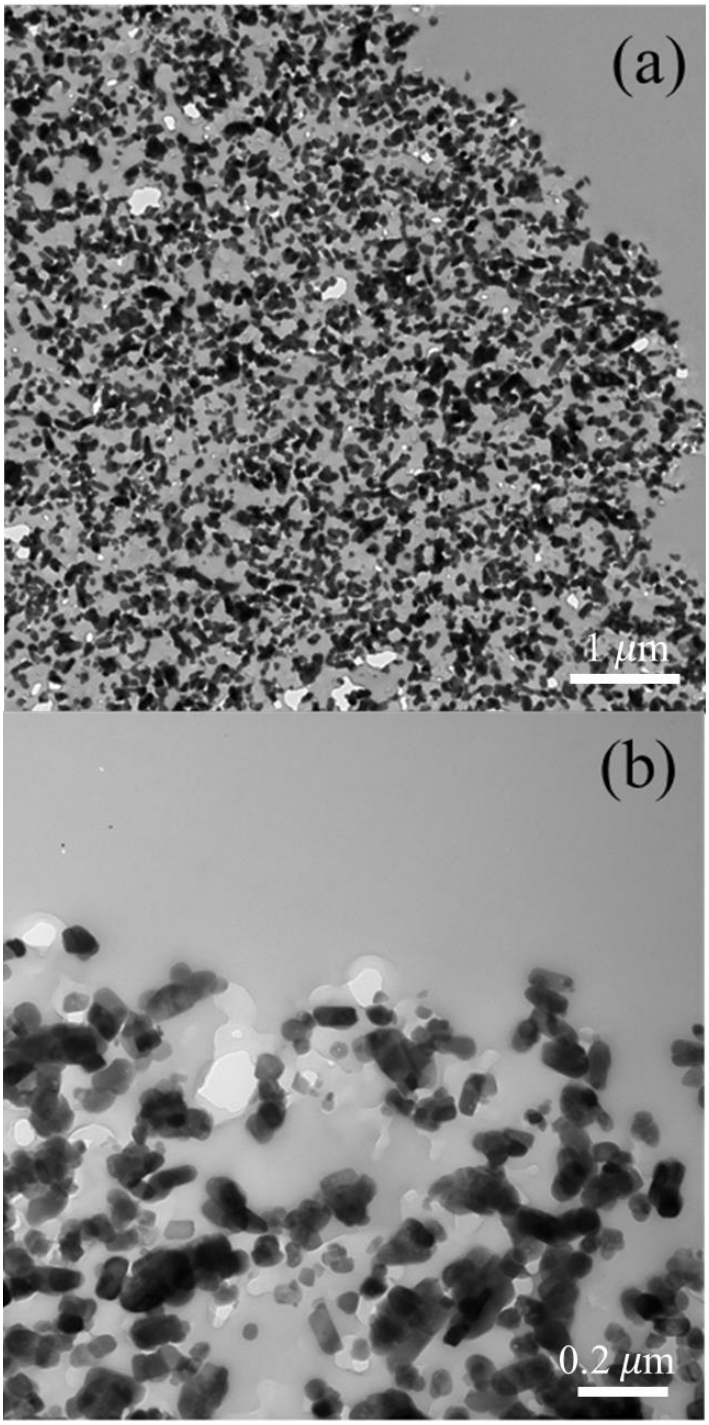

Figure 11 Representative TEM images of sections of CHT particles. (a) Structure near outer surface of particle at 10,000 magnification. (b) Structure near outer surface of particle at 40,000 magnification. Note the different scales for two images.

Figure 12 shows the iSEC elution peaks obtained for PEGs with different molecular masses between 300 and 35,000 Da. Dextran standards have been used by other iSEC experiments with different resins, but could not be used with CHT since they were found to bind (data not shown). As the molecular weight of the PEG probe increases, the retention decreases due to the greater steric exclusion. PEG 300 gains access to a large fraction of the particle volume, eluting at 0.8 CV. The extraparticle porosity obtained from the pressure drop measurements in Section 3.2.2.1 is shown by the vertical dash line.

The hydrodynamic radius of the PEG standards used was estimated using the following equation [40]:

$$r_{h,PEG} = 0.0191(MW)^{0.559} \tag{23}$$

where r_h is in nm.

Figure 13 shows the distribution coefficient, K_D, calculated from the data in **Figure 12** as a function of each solute hydrodynamic radius, r_h. Porosity and pore radii obtained from these data are shown in **Table 5**. The apparent pore size is consistent with the CHT TEM images (**Figure 11**). VLPs, which have an average hydrodynamic radius of 34 nm according to the DLS results, are likely to be at least partially excluded from the CHT pores. RNA, on the other hand, is likely to be able to diffuse into the CHT pore due to its small size and linear shape.

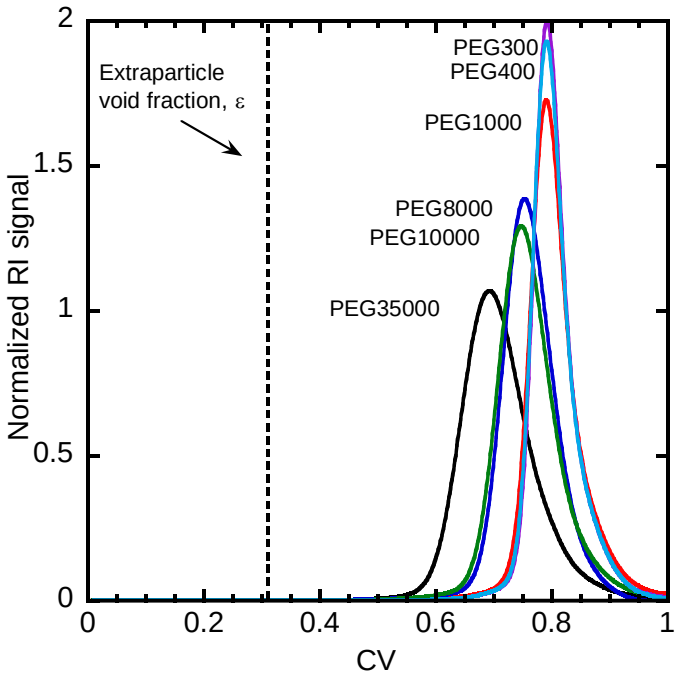

Figure 12 Chromatograms of PEG pulse injections from iSEC. Column length = 8.6 cm, mobile phase superficial velocity = 38 cm/h. The vertical dashed line represents the $\boldsymbol{\varepsilon}$.

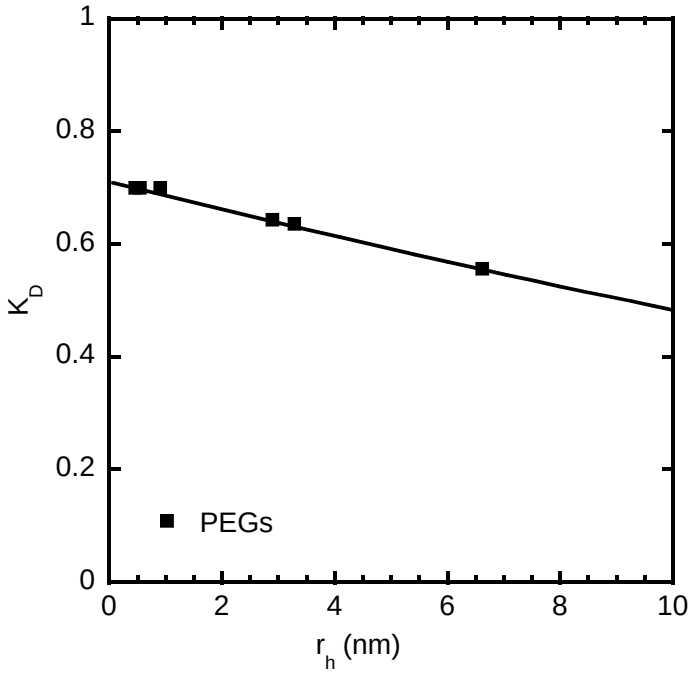

Figure 13 Distribution coefficient $\boldsymbol{K_D}$ for 300, 400, 1000, 8000, 10000, 35000 Da PEG standards plotted as a function of their hydrodynamic radii, $\boldsymbol{r_h}$. The line is calculated from eq. (16) using the parameters in Table 5.

Table 5 Summary of physical properties

Matrix	$\boldsymbol{\varepsilon}$	$\boldsymbol{\varepsilon_p}$	$\boldsymbol{\varepsilon_{total}}$	$\boldsymbol{r_{pore}\,(nm)}$
CHT II	0.31 ± 0.01	0.71 ± 0.01	0.80 ± 0.01	60 ± 1

4.2.2. Chromatographic Behavior

Figure 14 shows the linear gradient elution (LGE) chromatographic behaviors of VLP Type 18 and/or RNA on the CHT column. An increasing phosphate concentration over 20 CV was used for these experiments. VLP and RNA were both detected at 280 nm. A preliminary experiment has demonstrated that UV signals at 260 nm and 280 nm of RNA are similar. The eluted VLPs have a hydrodynamic radius of 32 nm based on DLS (**Table 1**). This size is equivalent to the original VLP size indicating that VLP conformation is unaffected by adsorption or elution steps. As the RNA sample is a heterogeneous mixture, a broad peak is obtained during elution. Since RNA has a large number of phosphate groups, it is expected to bind to the C-sites of the particles replacing the buffer phosphate ions. This mechanism is consistent with the RNA results which indicate that elution occurs at low phosphate concentrations. VLP elutes later. For insights into the binding mechanism of VLPs on CHT, an LGE experiment was conducted by increasing sodium chloride concentration which affects the electrostatic interactions. Even at high sodium chloride concentrations (2 M NaCl), no VLP could be eluted from the column (data not shown). This result suggests that binding of VLP involves chelation, such as carboxylate-calcium interaction, instead of pure ionic interactions. Elution requires displacers with stronger affinity for C-sites, such as phosphate, citrate or fluoride ions. The mixture elution behavior shown in **Figure 14** indicates that some RNA shares the same retention with VLP.

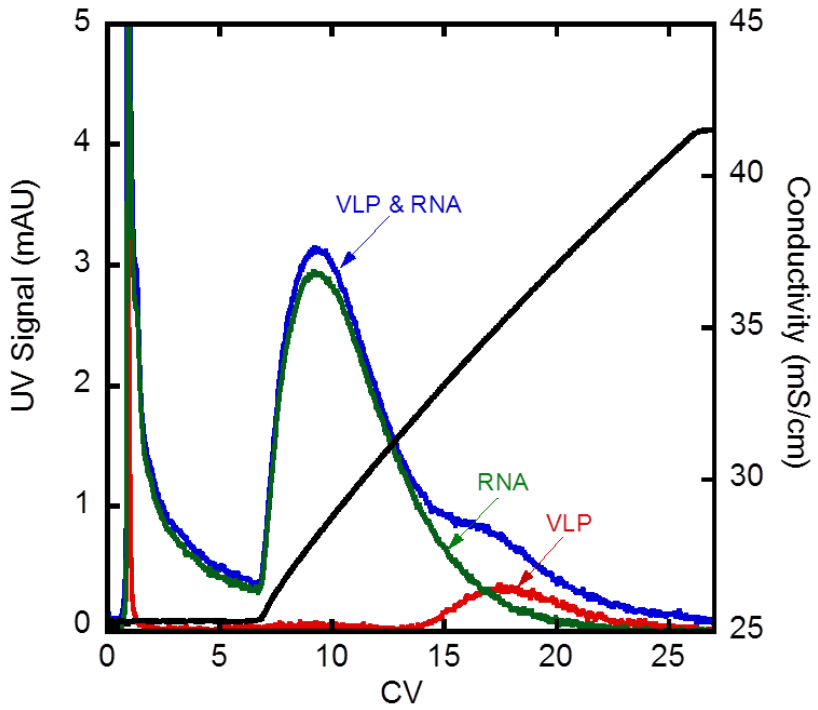

Figure 14 Overlaid elution chromatograms of VLP, RNA and a VLP/RNA mixture on CHT obtained by gradually increasing the buffer composition from 250 mM NaCl, 5 mM Na_2HPO_4 to 250 mM NaCl, 200 mM Na_2HPO_4. Both buffers are at pH 7.

4.2.3. RNA Adsorption

Figure 15 shows RNA adsorption isotherms on CHT under different conditions. By fitting the data with Langmuir isotherm model, the maximum binding capacity (q_m) and the equilibrium binding constant (*K*) were determined. These values are summarized in **Table 6**. As phosphate concentration increases, the maximum binding capacity is lower and the isotherm slope is shallower, which is consistent with the chromatographic behavior. At the highest phosphate concentration used (250 mM NaCl, 200 mM Na_2HPO_4), RNA binding is negligible. Another interesting behavior is that a higher NaCl concentration (1 M NaCl, 5 mM Na_2HPO_4) increases the maximum RNA binding capacity. This is likely caused by a reduction in repulsive forces between the P-sites and the phosphoryl groups of RNA.

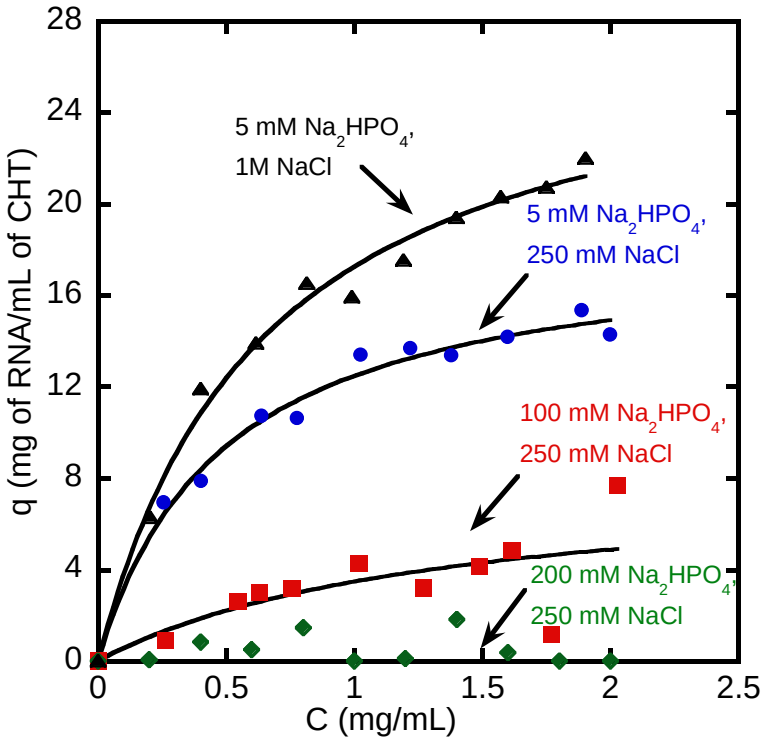

Figure 15 Adsorption isotherms of RNA on CHT particles in different sodium buffer at pH 7 and room temperature. Lines are based on the Langmuir isotherm model using the parameters in **Table 6**.

Figure 16 shows the CLSM images of the progress of adsorption of Alexa Fluor 488 green-labeled RNA over time. As seen in the images, RNA diffuses fairly quickly into the particles, attaining saturation in 15 to 30 min, as indicated by the nearly uniform fluorescence intensity. Similar trends are seen in 50 and 100 mM phosphate, although with much lower fluorescence intensity, consistent with the lower binding capacity in higher phosphate concentration seen in **Figure 16**.

Table 6 Maximum binding capacities and equilibrium constants from different adsorption conditions of RNA on CHT

C_{NaCl} (mM)	$C_{Na_2HPO_4}$ (mM)	q_m (g/L)	K (L/g)
1000	5	28.5 ± 1.34	1.5 ± 0.19
250	5	18.5 ± 0.78	2.0 ± 0.27
250	100	8.2 ± 5.7	0.7 ± 0.99
250	200	No binding	

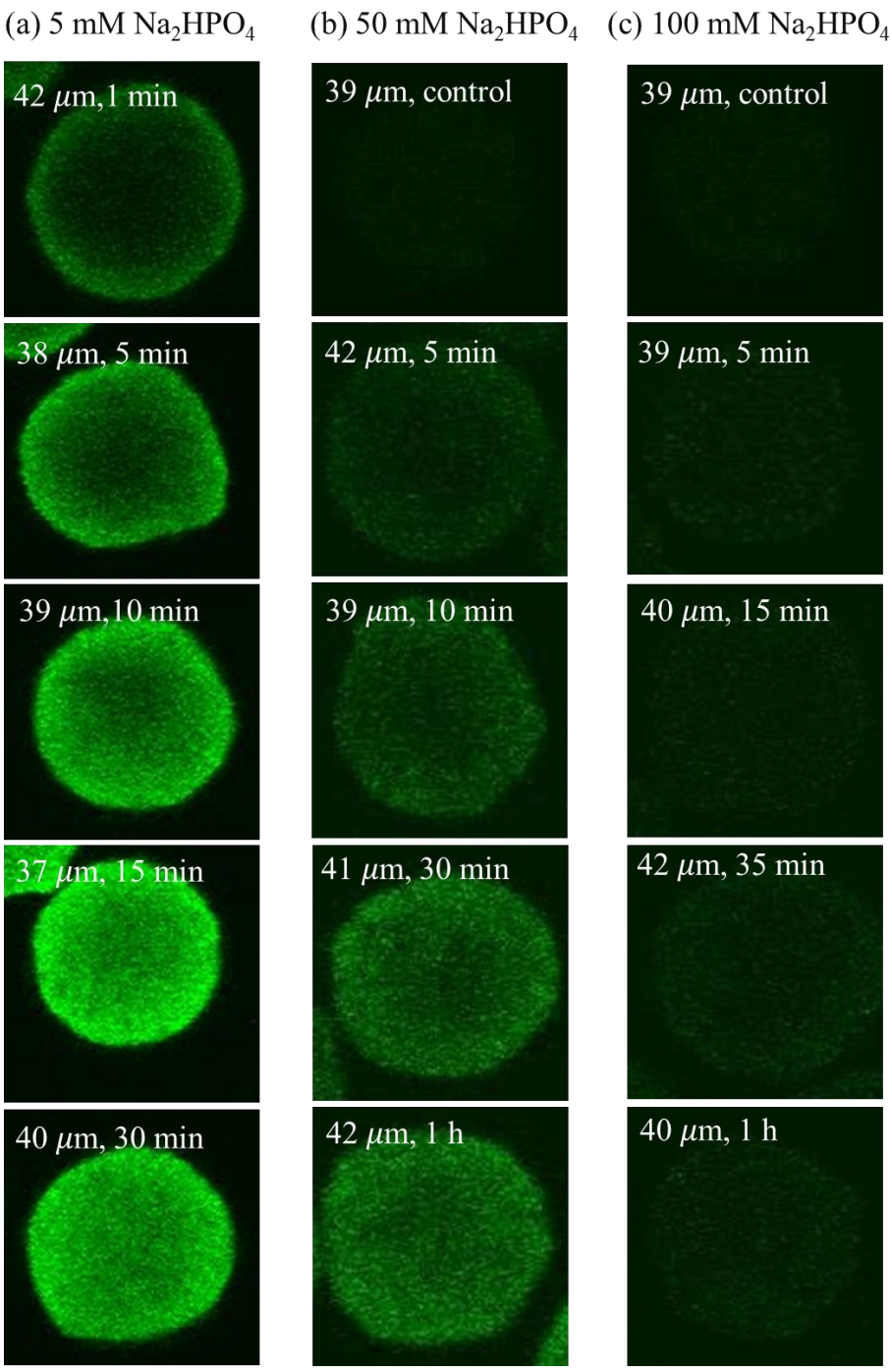

Figure 16 Representative CLSM images of batch adsorption of 2 mg/mL RNA on CHT particles in buffer of 250 mM NaCl with 5 mM (a), 50 mM (b), 100 mM (c) Na_2HPO_4. Different particles with diameters and adsorption durations are shown.

4.2.4. VLP Adsorption and Desorption

The VLP binding capacity was first estimated by assuming that it can only bind on the outer surface of the particle forming a monolayer. We assume that the VLPs are sphere that are bound on a hexagonal pattern on a flat surface. The binding capacity q (mg of VLP/mL of CHT) is estimated according to [41]:

$$q = \frac{2\pi}{r_{CHT}\sqrt{3}}\rho_{VLP}r_{VLP} \tag{24}$$

where ρ_{VLP} represents the mass of VLP protein per unit volume of VLP, and r_{VLP} is the radius of VLP and r_{CHT} is the radius of the CHT particles volume. The calculated q from this equation is 0.43 mg of VLP protein/mL of CHT. However, the experimental result shows the adsorption is 2.0 mg VLP protein/mL CHT. This larger experimental result indicates that VLP may not only bind as a monolayer on outer surface of the CHT but also on coarse surface or the pore mouths of CHT.

Figure 17 shows the CLSM images for Rhodamine Red-labeled VLP binding to CHT particles. It can be seen that the VLPs where able to bind only in a thin layer near the outer surface of the CHT particles even after 20 hours. This result shows that the CHT pores are likely to become clogged by the bound VLPs. Based on the iSEC results, the CHT pore radius is around 60 nm (**Table 5**), while the VLP radius, based on the DLS, is 32 to 37 nm (**Table 1**). As a result, the ratio λ_m of molecular size and pore size is between 0.5 and 0.6. In general, the effective pore diffusivity D_e is given by [42]:

$$D_e = \frac{\varepsilon_p D_0}{\tau_p}\psi_p \tag{25}$$

where D_0 is the free solution diffusivity, τ_p is the tortuosity factor and ψ_p is the diffusional hindrance coefficient, which in turn is related to λ_m. This relationship is illustrated in **Figure 18**, ψ_p is around 0.05 when λ_m = 0.5. This explains why VLP cannot diffuse inside the particle even the pore size is twice large than the VLP.

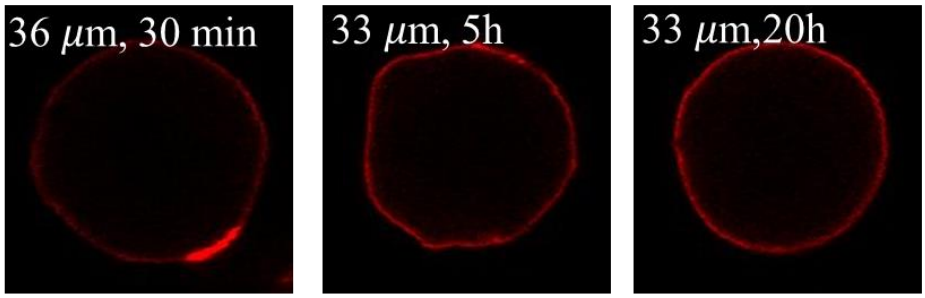

Figure 17 Representative CLSM images for batch adsorption of 0.2 mg/mL VLP at buffer of 5 mM Na_2HPO_4, 250 mM NaCl at pH 7. Different particles with diameters and adsorption durations are shown. VLP are resuspended in benzyl alcohol solution with DoL =0.03.

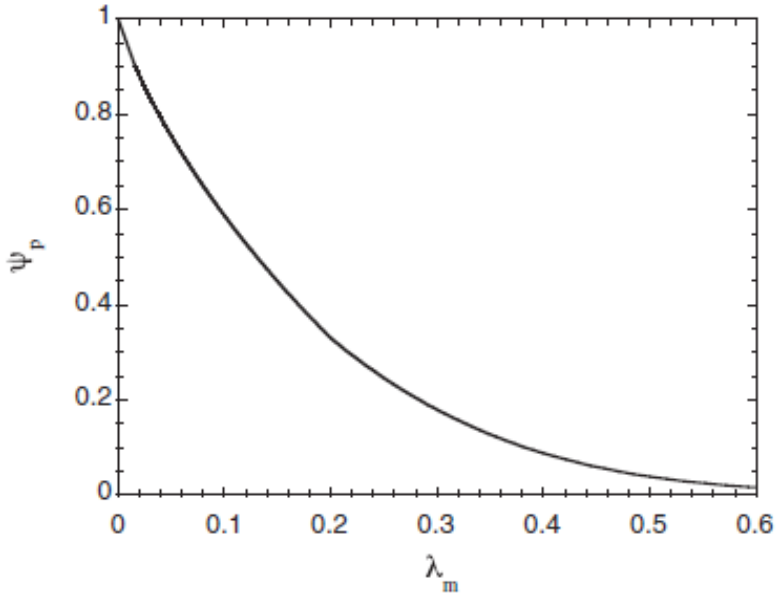

Figure 18 Diffusional hindrance coefficient plotted as a function of the ratio of molecular and pore radii [42].

Figure 19(a) and **Figure 19**(b) show the VLP adsorption behaviors in solution containing 50 and 100 mM Na_2HPO_4 respectively. The results are similar to those obtained in 5 mM phosphate suggesting that the VLP binding strength is still high for these conditions.

Figure 20 shows the VLP desorption from CHT particles. In this case, CHT particles were first incubated with 0.3 mg/mL VLP in the loading buffer (250 mM NaCl with 5 mM Na_2HPO_4) for 24 h. Then the particles were centrifuged at 5,000 rpm for 3 min to remove the protein solution and quickly immersed in a desorption buffer containing 250 mM NaCl with 200 mM Na_2HPO_4. Significant desorption can be observed within 5 min. However, even after 30 min, desorption is still incomplete with some labeled VLP remaining bound in a thin layer near the outer surface of the CHT particles.

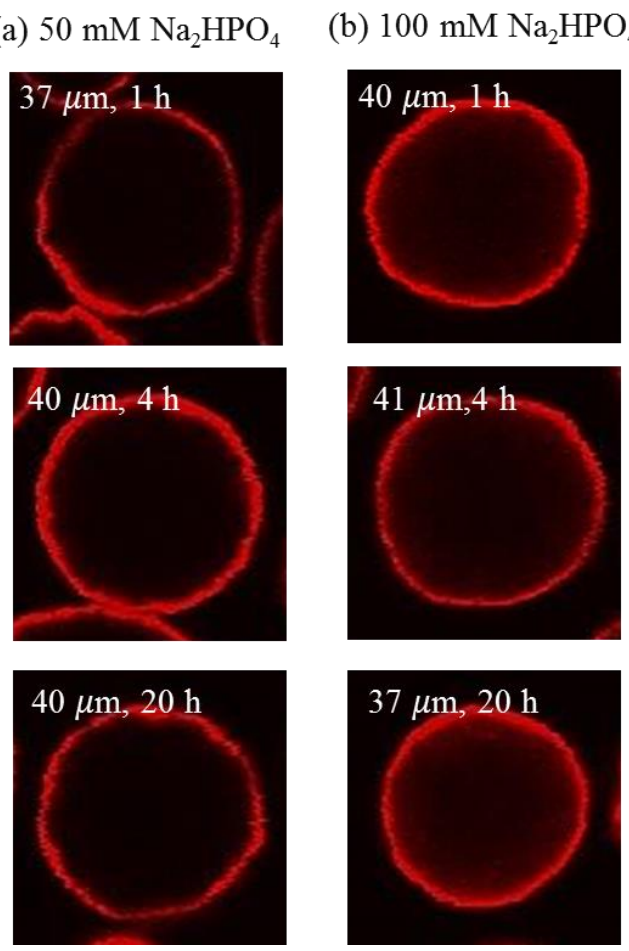

Figure 19 Representative CLSM images for batch adsorption of 0.2 mg/mL VLP in 50 mM Na_2HPO_4 (a), 100 mM Na2HPO4 (b) both with 250 mM NaCl at pH 7. Different particles with diameters and adsorption durations are shown in the image. VLP were resuspended in 50% sucrose solution with DoL =0.69.

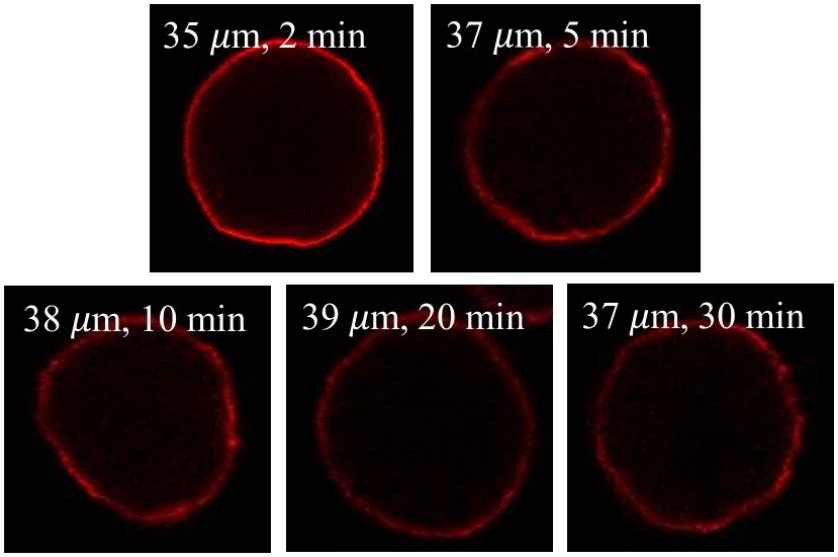

Figure 20 Representative CLSM images for batch desorption in 250 mM NaCl, 200 mM Na_2HPO_4 at pH 7 of VLP from CHT particles initially saturated in 250 mM NaCl, 5 mM Na_2HPO_4. Different particles with diameters and desorption durations are shown. VLP were resuspended in 50% sucrose solution with DoL =0.69.

4.2.5. Two-component Adsorption

Figure 21 shows CLSM images for co-adsorption of a VLP/RNA mixture in 250 mM NaCl, 5 mM Na_2HPO_4. As seen from this figure, the mixed components behave in the same way as in single component adsorption. Although VLP binding is limited to a thin layer near the particle outer surface, RNA is still being able to saturate the particle interior. The digital superposition of the two colors suggests that RNA does not bind in the VLP-saturated layer.

Figure 22 and **Figure 23** show images for RNA/VLP sequential adsorption. For the RNA-saturated particles, **Figure 22**, the VLP behaved in the same way as in co-adsorption indicating that VLP replaced the RNA bound near the particle outer surface. For the VLP-saturated CHT, **Figure 23**, RNA was able to diffuse to the center of the particles while the bound VLP was unaffected. These results indicate that bound VLP is not displaced by RNA and it does not completely block the pores (allowing RNA to still diffuse in).

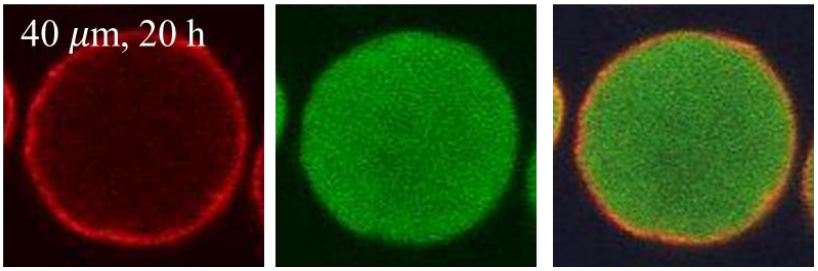

Figure 21 Representative CLSM images of VLP/RNA co-adsorption in 5 mM Na_2HPO_4, 250 mM NaCl. VLP is 0.2 mg/mL in red and RNA is 2 mg/mL in green. The rightmost image is the digital superposition of the two colors.

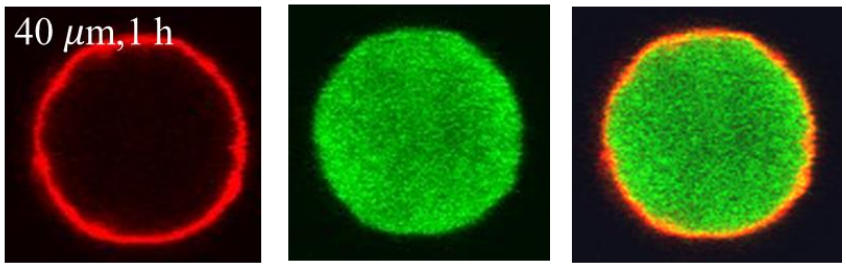

Figure 22 Representative CLSM images of sequential adsorption in 5 mM Na_2HPO_4, 250 mM NaCl. 2 mg/mL RNA presaturated CHT particles were then exposed to 0.2 mg/mL VLP.

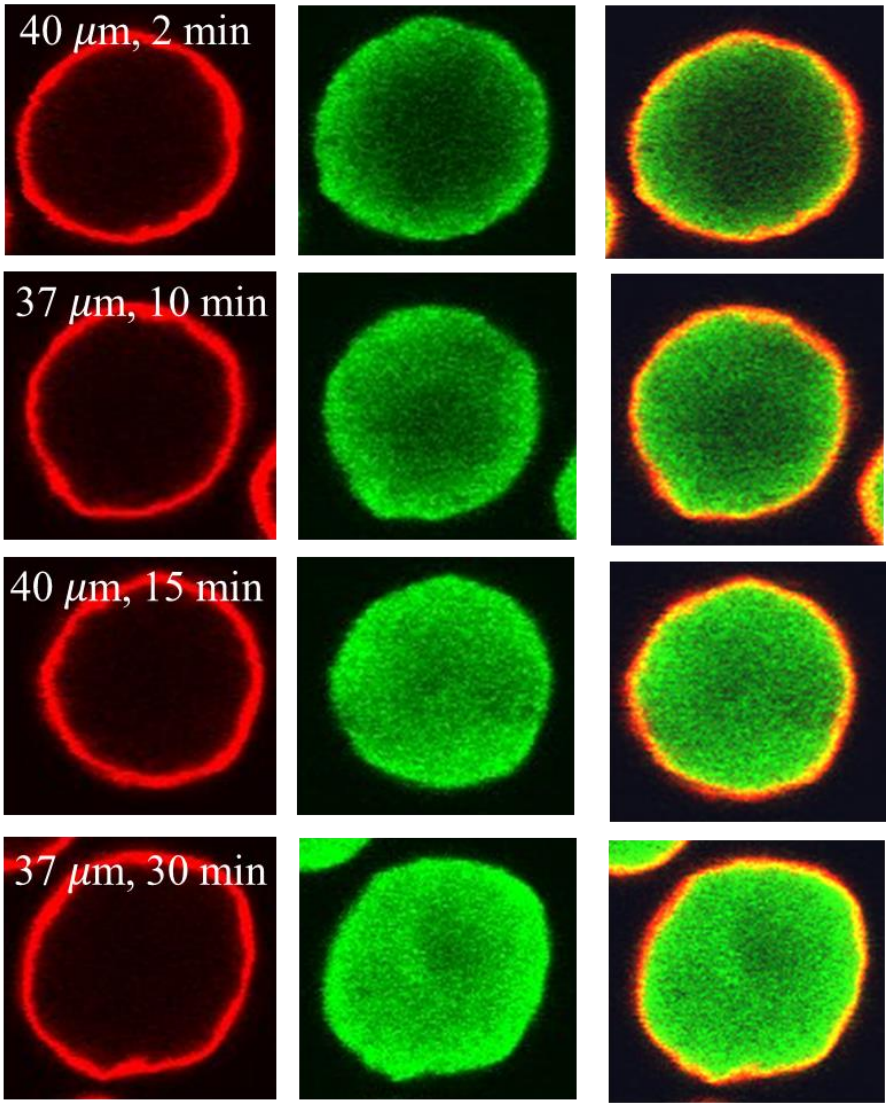

Figure 23 Representative CLSM images of sequential adsorption in 5 mM Na_2HPO_4, 250 mM NaCl. 0.2 mg/mL VLP presaturated CHT particles were then exposed to 2 mg/mL RNA.

4.2.6. RNA Localization Assays

The CLSM results show that RNA was able to bind throughout the CHT particles even though VLP binding was confined to a thin layer near the particle outer surface. An important question is whether RNA is associated with the bound VLP. The answer could be obtained by CLSM, but this would require fluorescent labeling of the associated RNA. The method used so far to

fluorescently label RNA requires high temperature, which is fine for RNA but which would destroy the VLP. Thus, an alternative fluorescent labeling protocol was sought to image any RNA associated with the bound VLP. The SYTO RNASelect green fluorescent stain assay [43] was thus introduced for this purpose. SYTO labeling is performed at room temperature and can be performed while the VLP is bond to the CHT particles. Additionally, SYTO labeling is RNA specific. To prove this last point, several proteins were put though the SYTO labeling procedure. **Figure 24** shows the fluorescence intensities obtained by labeling the different proteins and the VLPs. As seen from the figure, both the mAb and BSA gave very low intensity, while very high fluorescence was observed for the VLPs. We hypothesize that the high fluorescence obtained with the VLPs is due to RNA associated with the VLPs. The 10-fold dilution of the VLP sample gave 1/10 of the original fluorescence response indicating that fluorescence signal is also proportional to concentration.

Figure 25 shows CLSM images for adsorption of Type 18 VLP on the CHT particles in 250 mM NaCl, 5 mM Na_2HPO_4 on CHT. After contact with the VLP for 24 hours, the CHT particles were stained by SYTO RNASelect. The CLSM images show that significant green florescence is detected only in the region of the CHT particles where the VLPs bind. This result validates the hypothesis that RNA is associated with the VLPs and is not removed when the VLPs bind to CHT for these conditions.

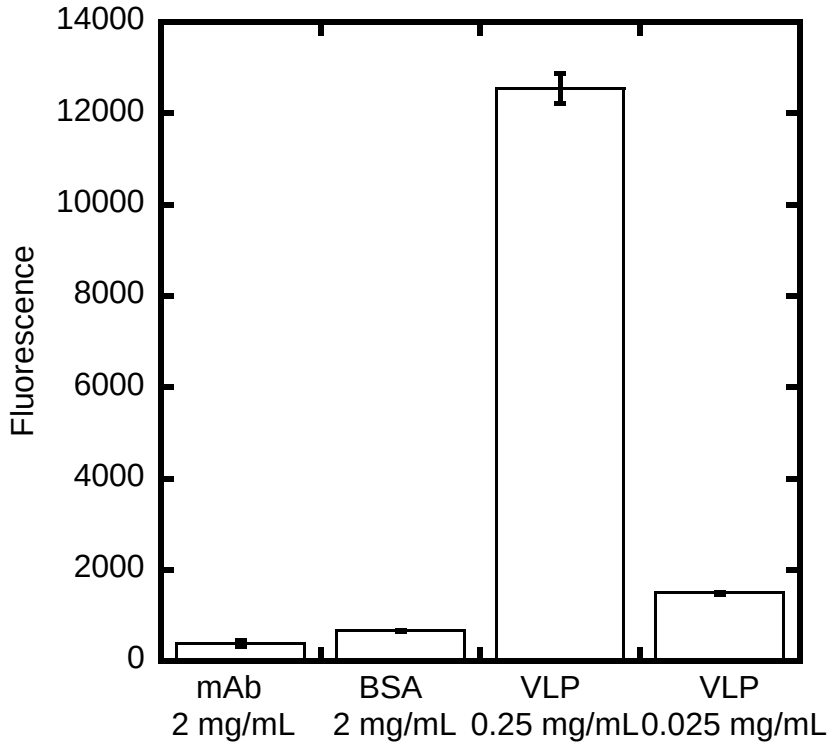

Figure 24 A selectivity test of SYTO RNASelect reagent. mAb (2 mg/mL), BSA (2 mg/mL), VLP Type 18 (0.25 mg/mL and 0.025 mg/mL) were stained by the RNASelect reagent for 20 min with the buffer of 250 mM NaCl, 5 mM Na_2HPO_4 at pH 7 in room temperature.

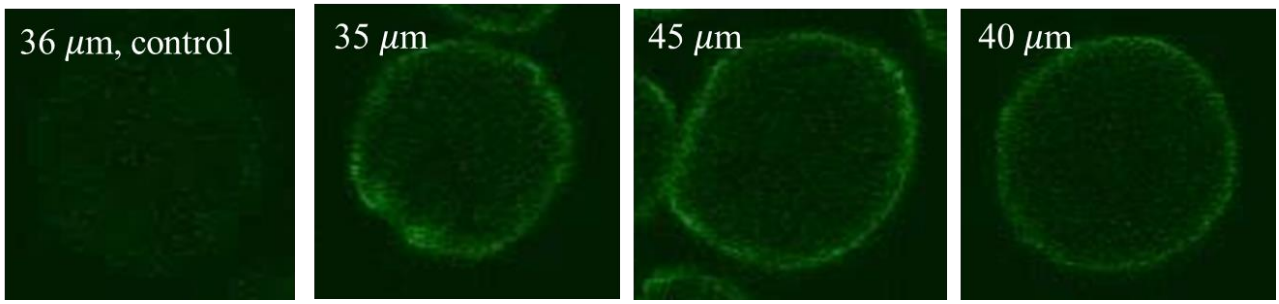

Figure 25 Representative CLSM images of VLP-saturated CHT staining by SYTO RNASelect for 20 min in 250 mM NaCl, 5 mM Na_2HPO_4 at pH 7. CHT particles were initially saturated with 0.2 mg/mL VLP in 250 mM NaCl, 5 mM Na_2HPO_4.

Chapter 5
Conclusions and Recommendation

5.1 Conclusions

5.1.1. RNA-VLP Association

This work has resulted in the development of a rapid, reliable and reproducible method to quantify the interaction between RNA and HPV VLPs using biolayer interferometry (BLI) with either a pre-functionalized RNA-biosensor or a VLP-biosensor.

With this method, association between RNA and Type 18 HPV-VLPs was confirmed. Kinetics and equilibrium constants were determined and found to depend on the type of VLP and the buffer composition. VLP Type 18 shows stronger association which is consistent with the difficulties encountered in practice in removing RNA from Type 18 preparations. The phosphate concentration in solution was found to weaken the VLP-RNA association.

5.1.2. Chromatography Behavior of RNA and VLP on CHT Type II

The structure of CHT Type II was characterized using transmission electron microscopy (TEM) and inverse size exclusion chromatography (iSEC). CHT Type II consists of 100-200 nm hydroxyapatite nanocrystals sintered to form nearly spherical particles, about 40 μm in diameter. The network of nanocrystals defines a pore structure with pores 50 to 200 nm in size which is readily accessible by RNA molecules.

Confocal laser scanning microscopy (CLSM) using fluorescently labeled RNA and VLPs. It shows that RNA can indeed diffuse rapidly in these pores and bind throughout the particle volume. Binding of VLPs is, however, limited to a thin layer near the CHT particle outer surface,

suggesting that the VLPs bound near the pore mouths prevent additional VLPs from diffusing into the interior of the particles. Similar trends are seen for co-adsorption and sequential adsorption experiments. During co-adsorption of VLP-RNA mixture, VLP binding is again restricted to a thin layer near the particle surface. RNA, however, is able to diffuse through the VLP-saturated layer rapidly saturating the area of the CHT particle that is not saturated with VLPs. Sequential adsorption experiments show that VLPs are able to bind on RNA saturated CHT particles as a result of the greater binding strength. RNA, on the other hand, cannot displace the pre-bound VLPs, but diffuses into the particle binding in the VLP-free region.

Desorption experiments with RNA-saturated particles, show that nearly quantitative desorption of RNA is possible by increasing the phosphate concentration. Even in high phosphate, however, desorption of VLPs for VLP-saturated CHT particles is incomplete. Desorption of CHT particles loaded with a RNA-VLP mixture show that at intermediate phosphate concentration, most of the RNA is removed while eventually all of the VLPs remain bound.

An experiment using *in situ* fluorescence labeling of the RNA associated with the VLPs bound to CHT without any additional RNA, shows that the associated RNA is confine to the same region of the CHT particle where the VLPs are bound. This result suggests that VLP-binding to CHT does not break the association at least at the low phosphate concentration used in this experiment.

5.2. Recommendations for Future Work

Although a significant association between VLP and RNA was observed, the mechanism of the interaction is still unclear. Further study will analyze the responses of synthetic RNA with specific sequences to determine the nucleotide binding preference. Other techniques such as saturation transfer difference-nuclear magnetic resonance (STD-NMR) should be used to provide

more information about the molecular recognition mechanisms [16]. Buffer composition effects need to be studied deeply; for example, high ionic-strength buffer without phosphate should be used to determine whether ionic-strength or the phosphate concentration weakens the association. Varying buffer pH should also be studied because protein net charge could be highly dependent upon pH. This assay would detect whether electrostatic forces are dominant in association mechanism.

These results provide an important insight when designing a purification step of VLP Type 18. The association may result in failure to remove the majority of RNA from the capture step since general buffer used here does not contain phosphate. Higher Na_2HPO_4 concentration is recommended in the capture step. Although BLI experiments show that RNA association is relatively weak under high Na_2HPO_4, a SYTO experiment should also be done to verify that RNA is not bound with VLP during CHT elution. Further study needs to be conducted in order to remove the co-eluted RNA. Increasing the binding capacity of VLP is one possible solution to this problem. Divalent cations, such as $CaCl_2$ and $MgCl_2$, are recommended in this step to strengthen the binding of VLP by the formation of additional bridges between the C-sites and the carboxyl groups. Another approach to improve adsorption of VLP on CHT is to choose adsorbent matrices with suitable structures. Future work will extend the adsorption studies to other candidates such as CHT XL, a new type of CHT with larger pore size.

Previous studies demonstrated that disassembly and reassembly facilitate VLP Type 6, 11 and 16 to form capsids with uniform size [44]. VLP Type 18 did not typically undergo self-disassembly and is insensitive to the traditional disassembly reagent, therefore, the whole disassembly and reassembly steps are absent for Type 18. This absence prevents the nuclease from removing any

residual contaminants which are still contained within the capsid. Future studies will investigate the presence of these containments such as internal residual RNA.

Reference

[1] Shi, L. *et al.* GARDASIL: prophylactic human papillomavirus vaccine development--from bench top to bed-side. *Clin. Pharmacol. Ther.* **81,** 259–264 (2007).

[2] Baek, J.-O., Seo, J.-W., Kim, I.-H. & Kim, C. H. Production and purification of human papillomavirus type 33 L1 virus-like particles from Spodoptera frugiperda 9 cells using two-step column chromatography. *Protein Expr. Purif.* **75,** 211–217 (2011).

[3] Gross G., HPV-vaccination against cervical carcinoma: will it really work? *Med. Microbiol. Immunol.* **196,** 121–125 (2007).

[4] Kirnbauer, R., Booy, F., Cheng, N., Lowy, D. R. & Schiller, J. T. Papillomavirus L1 major capsid protein self-assembles into virus-like particles that are highly immunogenic. *Proc. Natl. Acad. Sci. U. S. A.* **89,** 12180–12184 (1992).

[5] McCarthy, M. P., White, W. I., Palmer-Hill, F., Koenig, S. & Suzich, J. Quantitative disassembly and reassembly of human papillomavirus type 11 viruslike particles in vitro. *J. Virol.* **72,** 32–41 (1998).

[6] Park, M.-A., Kim, H. J. & Kim, H.-J. Optimum conditions for production and purification of human papillomavirus type 16 L1 protein from Saccharomyces cerevisiae. *Protein Expr. Purif.* **59**, 175–181 (2008).

[7] Buck, C.B., Trus, B.L. The papillomavirus virion: a machine built to hide molecular Achilles' heels. *Adv. Exp. Med. Biol.* **726**, 403–422 (2012).

[8] Aires K.A., Cianciarullo A.M., Carneiro S.M., Villa L.L., Boccardo E., Perez-Martinez G., Perez-Arellano I., Oliveira M.L. & Ho P.L. Production of human papillomavirus type 16

L1 virus-like particles by recombinant Lactobacillus casei cells, *Appl. Environ. Microbiol.* **72,** 745–752 (2006).

[9] Hofmann, K. J.,. Cook J. C, Joyce J. G., Brown D. R., Schultz L. D., George H. A., Rosolowsky M., Fife K. H. & Jansen K. U. Sequence determination of human papillomavirus type 6a and assembly of virus-like particles in Saccharomyces cerevisiae. *Virology* **209**:506–518 (1995).

[10] Kim, S. N., Jeong, H. S., Park, S. N. & Kim, H.-J. Purification and immunogenicity study of human papillomavirus type 16 L1 protein in Saccharomyces cerevisiae. *J. Virol. Methods* **139,** 24–30 (2007).

[11] Wu, Y., Simons, J., Hooson, S., Abraham, D. & Carta, G. Protein and virus-like particle adsorption on perfusion chromatography media. *J. Chromatogr. A* **1297,** 96–105 (2013).

[12] Bryan, J. T. Developing an HPV vaccine to prevent cervical cancer and genital warts. *Vaccine* **25,** 3001–6 (2007).

[13] Cook, J. C. *et al.* Purification of virus-like particles of recombinant human papillomavirus type 11 major capsid protein L1 from Saccharomyces cerevisiae. *Protein Expr. Purif.* **17,** 477–484 (1999).

[14] Jankowsky, E. & Harris, M. E. Specificity and nonspecificity in RNA-protein interactions. *Nat Rev Mol Cell Biol* **16,** 533–544 (2015).

[15] Hall, K. B. RNA-protein interactions. *Curr. Opin. Struct. Biol.* **12,** 283–288 (2002).

[16] Cruz, C., Cabrita, E. J. & Queiroz, J. A. Screening nucleotide binding to amino acid-coated supports by surface plasmon resonance and nuclear magnetic resonance. *Anal. Bioanal. Chem.* **401,** 983–993 (2011).

[17] Lee, M.-H. & Schedl, T. *RNA-binding proteins*. *WormBook* 1–13 (2006).

[18] Marenchino, M., Armbruster, D. W. & Hennig, M. Rapid and efficient purification of RNA-binding proteins: application to HIV-1 Rev. *Protein Expr. Purif.* **63,** 112–9 (2009).

[19] Alves, C. & Cunha, C. Electrophoretic Mobility Shift Assay: Analyzing Protein–Nucleic Acid Interactions. *Cdn.Intechopen.Com* (2012).

[20] Hégarat, N., François, J. C. & Praseuth, D. Modern tools for identification of nucleic acid-binding proteins. *Biochimie* **90,** 1265–1272 (2008).

[21] Howarth, M. *et al.* A monovalent streptavidin with a single femtomolar biotin binding site. *Nat. Methods* **3,** 267–73 (2006).

[22] Tiselius, A., Hjertén, S. & Levin, Ö. Protein chromatography on calcium phosphate columns. *Arch. Biochem. Biophys.* **65,** 132–155 (1956).

[23] Kawasaki, T., Takahashi, S. & Ikeda, K. Hydroxyapatite high-performance liquid chromatography: column performance for proteins. *Eur. J. Biochem.* **152,** 361–371 (1985).

[24] Gorbunoff, M. J. The interaction of proteins with hydroxyapatite. *Anal. Biochem.* **136,** 433–439 (1984).

[25] Chen, W. Y. *et al.* Studies of the interaction mechanism between single strand and double-strand DNA with hydroxyapatite by microcalorimetry and isotherm measurements. *Colloids Surfaces A Physicochem. Eng. Asp.* **295,** 274–283 (2007).

[26] Giovannini, R., Freitag, R. Purification of Antibodies by Chromatographic Methods. *Bioseparation* **9,** 359–368 (2000).

[27] Gagnon, P., Frost, R., Tunon, P. & Ogawa, T. CHT ^{TM} Ceramic Hydroxyapatite — A New Dimension in Chromatography of Biological Molecules. (2009).

[28] Tan, H. *et al.* Fiber-optic assay apparatus based on phase-shift interferometry. (2008).

[29] Shi, L. *et al.* Stabilization of human papillomavirus virus-like particles by non-ionic surfactants. *J. Pharm. Sci.* **94,** 1538–1551 (2005).

[30] Hartmann, R. K., Bindereif, A., Schön, A. & Westhof, E. *Handbook of RNA Biochemistry*. (2008).

[31] Edwards, P. R., Maule, C. H., Leatherbarrow, R. J. & Winzor, D. J. Second-order kinetic analysis of IAsys biosensor data: its use and applicability. *Anal. Biochem.* **263,** 1–12 (1998).

[32] Hagel L, Ostberg M, Andersson T. Apparent pore size distributions of chromatography media. *J Chromatogr A.***743.**33–42(1996)

[33] Zhang, S. *et al.* Structural and functional characteristics of virgin and fouled protein A MabSelect resin cycled in a monoclonal antibody purification process. *Biotechnol. Bioeng.* **113,** 367–375 (2015).

[34] Zhu, M. & Carta, G. Adsorption of polyethylene-glycolated bovine serum albumin on macroporous and polymer-grafted anion exchangers. *J. Chromatogr. A* **1326,** 29–38 (2014).

[35] Ratner, B. D. *et al. Biomedical Engineering e-Mega Reference.* (Academic Press, 2009)

[36] Celis, J. E. *Cell biology : a laboratory handbook*. (Elsevier Academic, 2006).

[37] Dantzler, J. Using the Octet RED with Virus-like Particles to Study Binding to Intact Membrane Proteins. in (2014).

[38] O'Brien, P. J. *et al.* The novel apolipoprotein a5 is present in human serum, is associated with VLDL, HDL, and chylomicrons, and circulates at very low concentrations compared with other apolipoproteins. *Clin. Chem.* **51,** 351–359 (2005).

[39] Abdiche, Y., Malashock, D., Pinkerton, A. & Pons, J. Determining kinetics and affinities of protein interactions using a parallel real-time label-free biosensor, the Octet. *Anal. Biochem.* **377,** 209–217 (2008).

[40] Fee, C. J. & Van Alstine, J. M. Prediction of the viscosity radius and the size exclusion chromatography behavior of PEGylated proteins. *Bioconjug. Chem.* **15,** 1304–1313 (2004).

[41] Carta, G. & Jungbauer, A. *Protein Chromatography Short Course*. (2016).

[42] Carta, G. & Jungbauer, A. *Protein Chromatography*. (2010).

[43] Savas, J. N. *et al.* A role for Huntington disease protein in dendritic RNA granules. *J. Biol. Chem.* **285,** 13142–13153 (2010).

[44] Mach, H *et al.* Disassembly and reassembly of yeast-derived recombinant human papillomavirus virus-like particles (HPV VLPs). *J. Pharm. Sci.* **95**, 2195-2206 (2006).